Linking the selectivity of varying surface phases of a real palladium catalyst toward specific methane oxidation pathways with Ambient Pressure X-ray Photoelectron Spectroscopy
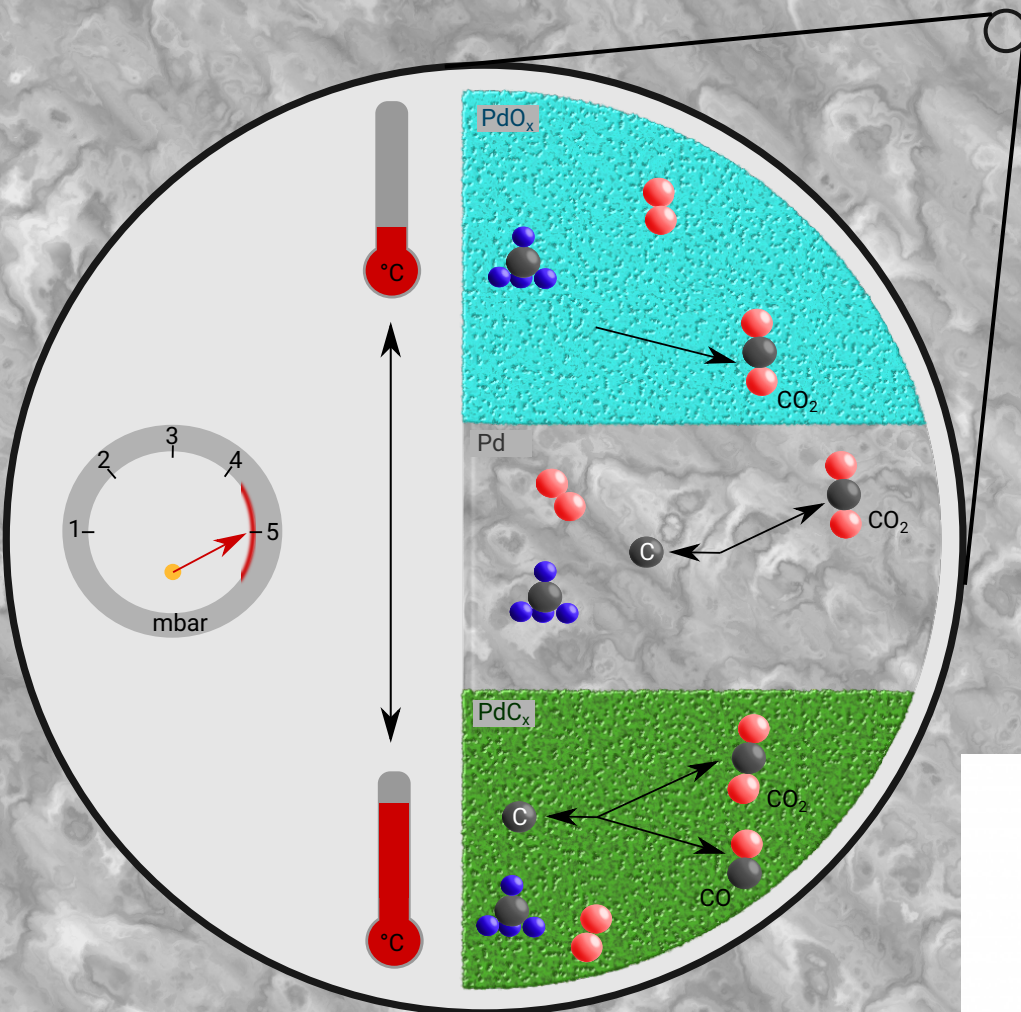
Ulrike Küst

Thesis submitted for the degree of Master of Science

Project duration: 6 months

Supervisor: Jan Knudsen   Co-Supervisor: Johan Gustafson

Department of Physics - Division of Synchrotron Radiation Physics

March 2023

ABSTRACT

The study of heterogeneous catalysis, especially within methane oxidation, is of high importance in order to more efficiently remove unburned methane from bio-fuel exhausts. This is relevant as bio-fuel engines will replace those driven by fossil fuels in the coming decades. This thesis contributes to the understanding of that reaction in a 5 mbar environmental pressure regime over a polycrystalline, rough palladium catalyst. The work thus bridges both, the materials gap by using a *real* catalyst and the pressure gap by approaching industrial pressures. Various surface phase transitions between oxide, carbide, and metallic surfaces were induced by ramping the catalyst temperature between 350 °C and 585 °C. Meanwhile, changes in the products of the methane oxidation were observed with time-resolved Ambient Pressure X-ray Photoelectron Spectroscopy (tr-APXPS), it hence became possible to specifically relate certain surface phases to complete or partial oxidation of methane as well as carbon deposition on the surface. These results, especially the fact that carbon deposition already takes place when there is still oxide at the surface, might prove highly relevant for industrial applications. Furthermore, applying temperature ramps to enforce transitions in the catalyst's surface phase is a novelty first applied in the realm of this thesis. The successes of this technique open up possibilities for future research in catalysis. These contributions will, in the long run, help to fabricate better catalysts for bio-fuelled engines whose development will help transition to a more sustainable lifestyle.

ABBREVIATIONS

XPS   X-ray Photoelectron Spectroscopy

APXPS   Ambient Pressure X-Ray Photoelectron Spectroscopy

UHV   Ultra High Vacuum

AP   Ambient Pressure

tr   time resolved

MTL   Mass Transfer Limit

QMS   Quadropole Mass Spectrometer

MCP   Multi Channel Plate

TOF   TurnOver Frequency

SXRD   Surface X-Ray Diffraction

PLIF   Planar Laser-Induced Fluorescence

SOR   Surface Optical Reflectance

UPS   Ultraviolet Photoelectron Spectroscopy

HAXPES   HArd X-ray PhotoElectron Spectroscopy

Contents

1. INTRODUCTION

As fossil fuels have both only a limited supply and a huge impact on climate, alternatives have to be found. One solution to this problem is the use of biogas. After the combustion of bio-fuels, the exhaust still contains methane which has a much higher greenhouse gas effect than carbon dioxide [1]. Hence, it is important to further process that methane into something less harmful to the environment and maybe even useful for industrial purposes. One possibility for this is the complete oxidation, or complete combustion, into water and carbon dioxide, and another partial combustion into syn-gas, for instance. These reactions, however, have a high activation energy due to the high intra-molecular bond strength of methane [2]. Thus, a strong catalyst such as palladium is needed. A technique that can be used to study these catalysts is Ambient Pressure X-ray Photoelectron Spectroscopy (APXPS) with which it is, in contrast to most surface-sensitive techniques, possible to have a gas surrounding the solid catalyst [3]. Meanwhile, the surface and the local gas composition in the vicinity of the surface can be probed, studying the reaction as it happens.

Two issues often mentioned when conducting research in heterogeneous catalysis, i.e. placing for instance a solid catalyst in a gaseous environment, are the material and pressure gap [4]. The material gap expresses that most industrial catalysts do not consist of well-defined surfaces but rather of polycrystals, i.e. small domains of varying surface orientations while surface science experiments usually are conducted on single-crystal surfaces. The pressure gap points to the fact that surface science experiments are often carried out at low pressures while the industry operates at pressures of several bars. The favored, most active surface phase, however, can vary significantly when passing through various pressure regimes or surface phases.

Furthermore, most research in heterogeneous catalysis focuses on the active site of the catalyst or the most active surface phase, sometimes even stating the specific oxidation mechanism of methane. To my knowledge, though, the oxidation mechanism has not been observed in dependence on a surface phase changing over time measuring with high temporal resolution.

In order to fill these knowledge gaps, the experiments conducted here study the model system of methane oxidation on a real palladium catalyst to bridge the materials gap at a pressure of a few millibars to reduce the pressure gap. That means that a formerly well-defined Pd(100) single crystal surface was roughened and oxides and carbides were formed. In the experiments, a temperature ramp is applied to the catalyst to vary the surface phase and the system is observed with time-resolved APXPS (tr-APXPS).

First, the model reaction was studied in a balanced gas environment, i.e. using the same flow of methane and oxygen. The temperature ramp applied to the catalyst results in oxides of varying thickness. In a second study, the catalyst was placed in a highly methane-rich environment, studying the same reaction for different surface phases, namely carbide, metallic, or oxide surfaces. Again, temperature ramps were used to induce surface phase transitions. These temperature-ramp-induced changes in the surface phase cause changes in the amount of methane that is processed via complete combustion, thus forming CO_2 and H_2O, partial combustion, resulting in CO and H_2O formation, or carbon deposition on the surface. This

reaction pathway profile, i.e. how much reactant is processed via which reaction channel, is then observable in the tr-APXPS spectra. Therefore, it is possible to relate the surface phase to the profile of reaction pathways.

In the analysis of the described experiments, a strong selectivity of certain surface phases toward a specific reaction pathway is found. Here, the oxide-covered surface is found to only process methane via complete combustion. The metallic Pd surface oxidizes methane completely as well, an increasing carbon deposition is observed, however. Finally, the carbide surface showed all possible reaction pathways, i.e. complete and partial combustion as well as carbon deposition.

Overall, the thesis is going to contribute to answering some of the major questions in carbohydrate oxidation over noble metal catalysts such as which surface phase results in which oxidation channel. As this is studied with high time resolution (0.2 s), even the properties of short-lived surface phases can be evaluated. This entails the possibility of a vast amount of industrial applications such as the development of a suitable catalyst for biogas engines.

2. THEORY

2.1. Heterogeneous catalysis

A surface in the common understanding of surface science is the truncation of a crystal. The direction of this truncation can be described by the so-called Miller indices which, together with the crystal geometry, uniquely define the structure of a surface. An example is the (100) surface of a face-centered-cubic (fcc) crystal such as palladium.

If a gas molecule interacts with such a surface, two different kinds of adsorption are usually differentiated. Depending on the strength of the bond that is formed between the adsorbate and the surface, one talks about physisorption or chemisorption. The prior is defined as a weak interaction. Instead, chemisorption is characterized by the formation of chemical bonds. Furthermore, the low equilibrium distances between the surface and the adsorbates define special, so-called, adsorption sites at the surface where adsorbates are preferably situated. This can then result in the formation of an adsorbate superstructure on top of the surface. The preferred adsorption site, and hence the preferred superstructure, is dependent on the environmental pressure and temperature, as those parameters define the diffusion rate of the adsorbates across the surface [5]. Thus, restructuring is either enhanced or inhibited.

The essence of heterogeneous catalysis is, that, in some cases, the bond between the adsorbates and the surface is even stronger than the intra-molecular bonds which leads to a dissociation of the molecule. Afterward, the atoms, that formerly belonged to the molecule form other molecules on the surface. Thus, the presence of the surface lowers the activation energy E_a for the reaction, sometimes through several steps in between, such as the dissociation of liquid or gaseous molecules while the surface is not altered in the process. This effect is shown in Figure 1 where the presence of the catalyst facilitates the reaction of the components X and Y to product Z. The effect of temperature T on the conversion rate k of this reaction is then described by the Arrhenius equation

$$k = A \times e^{-\frac{E_a}{k_B \times T}} \tag{1}$$

where A is some pre-factor and k_B the Boltzmann constant.
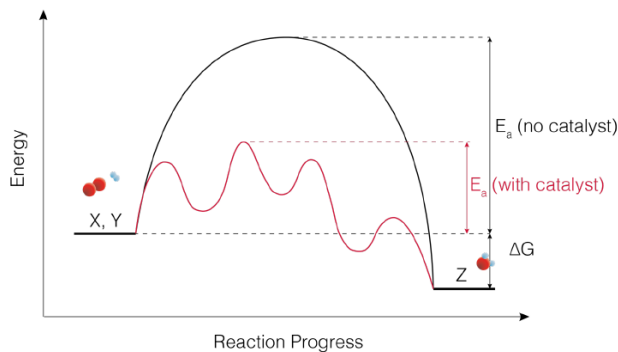
Figure 1: ***Energy along the reaction coordinate*** *including the initial activation energy and the lowered energy barriers due to the presence of the catalyst's surface. The figure is taken from [5].*

2.2. X-ray Photoelectron Spectroscopy (XPS)

To study and understand surface-mediated reactions, the chemical composition of the surface needs to be characterized. Conventionally Infrared Spectroscopy, X-ray Absorption Near-Edge Structure, or Extended X-ray Absorption Fine Structure have been used to study catalysts [6]. Since these are bulk-sensitive techniques, however, they provide little information about the surface structure of the catalyst. Therefore, the need for a surface-sensitive method arose which was met by the group of Kai Siegbahn at Uppsala University in the 1960s [3]. "For his contribution to the development of high-resolution electron spectroscopy" he was then awarded the Nobel Prize in Physics in 1981.

In X-ray Photoelectron Spectroscopy (XPS), the sample is irradiated with monochromatic X-rays which then leads to the emittance of photoelectrons if the energy of the incoming light is larger than the work function of the sample. If the photon energy is significantly higher than the sample work function, electrons can be removed from the core levels of the solid. Detecting and analyzing these photoelectrons is called core-level spectroscopy. In contrast to that, valence-band spectroscopy removes electrons from the valence band which makes it possible to obtain information about the electronic structure.

The kinetic energy of the photoelectrons (KE) that is measured in the electron spectrometer [6] needs to be transformed into the energy of the core level the electron has been removed from. This energy, usually called binding energy (BE), is obtained via the relation

$$BE = h\nu - KE \quad . \tag{2}$$

This binding energy then needs to be calibrated, a process which is described in the section about Fermi edge calibration 4.2. As core electrons do not extensively participate in chemical bonding, their binding energy is a fingerprint of the respective atom, which, however, is slightly shifted depending on the chemical bonds, the so-called chemical shift [5]. The emerging core hole then calls for relaxation processes such as the emission of an Auger electron or fluorescence. These signals can also be used to do spectroscopy on samples, e.g. Auger spectroscopy which is more sensitive to the chemical environment the atom is situated in [5].

8

There are several advantages of using electrons to analyze the surface over the use of photons or ions for instance. First, electrons are easily focused and their energy is tunable without much effort. They are simple to detect and count, thus, the instrumentation is easy to handle and comparably cheap [7]. The main advantage, however, is the short escape depth of electrons in matter, leading to a high surface sensitivity. The inelastic mean free path is a measure of the strong interactions of electrons with matter. As the electron distribution in most solids can be described as a free electron gas, the interactions between the electron beam and the solid are roughly similar for all materials and can be described by the so-called universal curve which is presented in Figure 2.
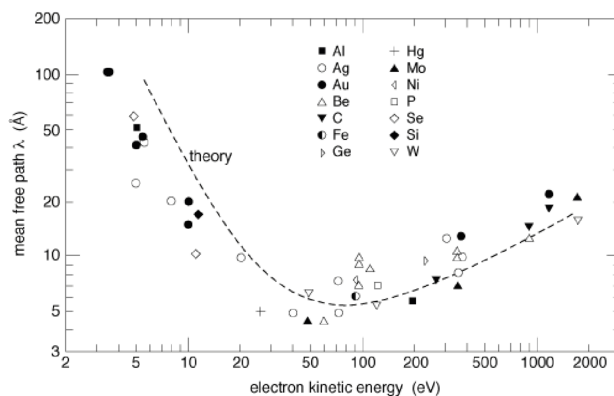
Figure 2: ***Universal curve** for the mean-free-path of electrons travelling through matter. The figure is taken from [5].*

Thus, at low electron kinetic energies around 100 eV, the interaction between electrons and atoms is rather strong for all elements [8]. This low mean free path is simultaneously also one of the main disadvantages of the method. It requires atomically clean surfaces and an Ultra High Vacuum (UHV) environment for the measurement [7]. This UHV requirement is a downside for the investigation of processes that require the presence of a phase interface. This is the case for example in heterogeneous catalysis [3].

Investigating the chemical nature of surfaces makes XPS an ideally suited technique when observing catalysts. It is important to obtain information about the surface as this is where the reaction between two materials takes place. Furthermore, one of the main goals in catalysis research is to determine the relationship between surface structure or chemical composition and the activity of the catalyst [6]. Using XPS, this is done by comparing the surface before and after the catalyst's participation in the reaction. Unfortunately, the observed surface phase in ex-situ experiments does not necessarily represent the in-situ surface phase. Therefore, much information about intermediate steps is lost [6].

For this reason, the interest in developing a method that would make observations of, e.g. heterogeneous catalysis, possible grew after the invention of XPS. And again, in the early 1970s, Kai Siegbahn's group at Uppsala University developed the first instruments making Ambient Pressure XPS (APXPS) possible [8].

2.3. Ambient Pressure X-ray Photoelectron Spectroscopy (APXPS)

The difficulty in measuring surfaces with electrons in a gaseous environment is in the small electron mean free path in matter. Therefore, a breakthrough in APXPS was achieved in the late 1990s and early 2000s with the introduction of the technique to synchrotron light sources [3]. The high intensity of the light produced there leads to a high photoelectron intensity which improves the signal-to-noise ratio in the measurement dramatically even after losses due to scattering or absorption of electrons in the gas phase. Another important improvement was the invention of electrostatic focusing, which, together with differential pumping stages that were already invented earlier, made it possible to rapidly reduce the environmental pressure. That minimizes the loss of electrons, again improving the signal-to-noise ratio [3].

The general approach of instrumentation is common to all APXPS setups [6] and can be seen in Figure 3. The sample is placed in a high-pressure cell, e.g. 5 mbar total pressure, and the X-rays are passing through a several 10 nm thick window that is transparent for this high energy radiation, e.g. silicon-nitride. The window is installed in order to keep the high pressure in the cell and the UHV conditions in the X-rays source [6]. A cone-shaped nozzle is placed above the sample surface. As the opening of the nozzle above the surface is very small, the region behind the nozzle can be kept at a 100 times lower pressure compared to the experimental cell [9]. In that region, a Quadropole Mass Spectrometer (QMS) can measure the gas composition which is in opposition to the APXPS measurement position that is located directly at the surface. Subsequent to the nozzle, there are several electrostatic lenses that focus the electrons, increasing the overall transmission of electrons through the system [6].
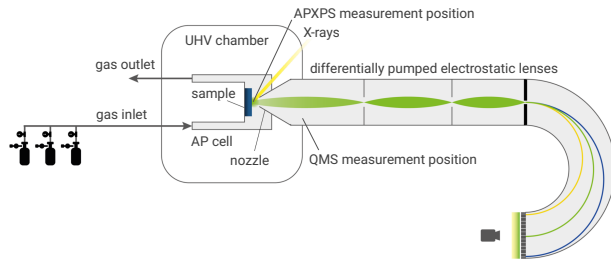
Figure 3: *Common APXPS setup which was also used during the measurements in this thesis. The figure is adapted from [5].*

After the electrons passed several pumping stages, reducing the pressure by approximately a factor of 100 every time, they reach the electron analyzer which operates at UHV pressures. There, they pass through a space in between hemispherical plates that set up an electric field that steers the electrons, depending on their kinetic energy, toward a Multi Channel Plate (MCP). That is shown by the differently colored lines in the analyzer in Figure 3 which indicate the trajectory of electrons with varying kinetic energies. Behind the MCP, a phosphorous screen visualizes the impinging electrons which is observed by a camera. This, most common, analyzer is the so-called Spherical Deflection Analyzer. Before entering the analyzer, a pre-retardation stage [7] decelerates all electrons. This is done so, that a previously

set kinetic energy is slowed down to the desired pass energy E_p. Accordingly, all other electrons are slowed down as well. As the detector can detect photon energies in the range of 10% of E_p, lower pass energies result in a better energy resolution. At the same time, however, E_p^2 is proportional to the signal intensity, thus, a compromise needs to be found. Usually, pass energies of 200 eV are chosen. Accordingly, the initial photon energy needs to be chosen in a way that the desired photoelectrons have at least a kinetic energy of roughly 200 eV.

Even though the pressures that can be reached with this setup are limited to a few mbar, and thus far from industrial conditions, they are high enough to observe dynamic developments on the surface monitoring reactions between the gas phase and the surface in the experimental chamber [9]. This approach narrows the pressure gap, often observed when studying well-prepared surfaces in UHV and comparing the results with industrial processes under high pressures [6]. There, due to different environmental conditions, other reaction paths can be preferred altering the final result of the reaction significantly.

## 2.4. Model system: Methane oxidation

In heterogeneous catalysis, the catalyst's functionality usually depends on several environmental conditions such as temperature or partial pressure of the reactants, but also on the surface phase. The number of reaction turnovers per surface site and time unit is usually referred to as turnover frequency (TOF). However, also the formation of new surface phases can happen due to changes in the environment. These new surface phases can then again have different activities and even facilitate other reaction channels.

Discussing the general properties of catalytic combustion, two important points in the reaction scheme when ramping up the temperature of the catalyst are the so-called light-off temperature and the temperature where the reaction starts to be mass transfer limited. At the light-off temperature, the catalyst is active for facilitating the desired reaction. When the temperature of the catalyst is increased further, the TOF increases until it is so high that eventually the frequency is limited by the amount of supply gas reaching the surface. This situation is then referred to as a mass transfer limit (MTL) of the gas in short supply. Within this thesis, the term conversion rate is used to describe the methane conversion or water production rate of the catalyst at a given temperature and surface phase.

For reactions with only one possible reaction pathway, CO oxidation, for instance, the conversion rate will be constant once the MTL is reached, however much the temperature is increased after that. Instead, for reactions with several possible reaction pathways, such as for methane oxidation, those pathways that use a lower amount of oxygen will be increasingly favored if oxygen is in short supply. Possible reaction pathways for methane oxidation, with decreasing amounts of processed oxygen atoms, are the complete combustion
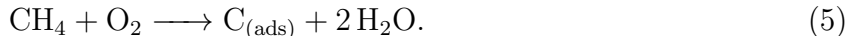
$$CH_4 + 2\,O_2 \longrightarrow CO_2 + 2\,H_2O \tag{3}$$

or the partial combustion of methane

$$CH_4 + \frac{3}{2}\,O_2 \longrightarrow CO + 2\,H_2O \tag{4}$$
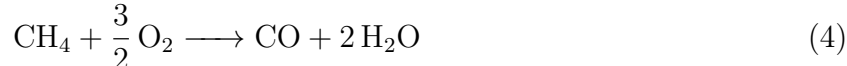
as well as carbon depletion on the surface

$$CH_4 + O_2 \longrightarrow C_{(ads)} + 2\,H_2O. \tag{5}$$

That means that for methane oxidation, even in the MTL, changes in the reaction pathway profile can be expected.

In general, many noble metals seem to be good catalysts for methane oxidation. Especially Palladium, however, is often used as it has been reported to be an outstanding catalyst for this reaction [6]. The reaction mechanism for methane oxidation over a Pd metal is the so-called Mars-Van Krevelen mechanism. It is used to describe the kinetics of hydrocarbon oxidation over noble metals and states that an adsorbed molecule reacts with a pre-existing reconstructed surface phase such as an oxide or a carbide. Thus, the process observed is a simultaneous oxidation and re-oxidation of the surface [10].

2.5. Temperature Ramps and Time Resolution
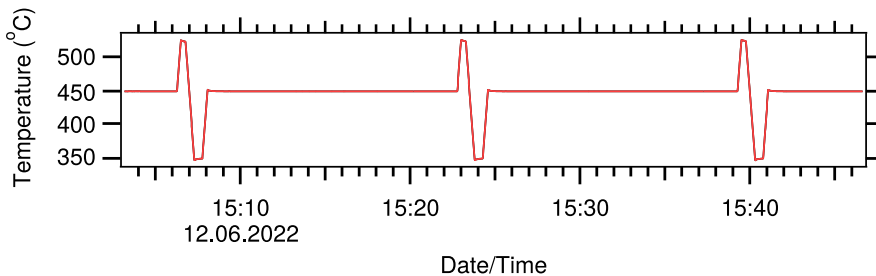
Figure 4: ***Example of a series of temperature ramps*** *that are applied to the catalyst material. This example shows three ramps of the following temperature pattern: With a 5 °C/s heating rate, a final temperature of 525 °C is set. After waiting for 30 s to also actually reach that temperature, 350 °C is set. After a waiting time of 60 s, the temperature is set to go to 450 °C. With these settings, a 900 s waiting time is passed.*

In the experiments in this thesis, temperature modulation of the catalyst material is used to achieve transitions of the surface phase. Previously, this has, for instance, been done by altering the gas composition around the catalyst [11]. These gas pulses, however, are rather slow [12], and only reach the surface in a diffuse way, i.e. the gas pulse does not reach the whole surface at the same, sharp point in time. This can be problematic, considering that the reactions at the surface could happen in short time frames that then cannot be resolved due to these blurred time structures provided by gas composition pulses. Therefore, the improvement of temporal resolution provided by in situ characterization methods is of increasing importance in order to understand the underlying reaction mechanisms in a better way [13].

In contrast to the poor time resolution of gas composition pulses, temperature ramps can be applied directly to the catalyst, achieving immediate effects that can be directly coupled to the current catalyst's temperature. This makes it possible, to study the catalyst in much more detail, i.e. with a much higher time resolution.

3. Setup

The experiments in this thesis study methane oxidation on a palladium sample. The sample surface has been prepared to be rough, and partly covered by oxides and carbides. This was achieved by several exposures of the catalyst to oxygen and methane. That reportedly roughens the surface [14], [15] and, over time, turns the crystalline sample into a polycrystalline structure. Conducting research on this crystal narrows the material gap often experienced in catalysis science where catalysts are studied under ideal conditions and with single crystals which is very different from the usual operating conditions.

The experiments were conducted at the soft X-ray beamline HIPPIE at the 3 GeV electron storage ring of the MAX IV Laboratory in Lund, Sweden. The beamline is dedicated to Ambient-Pressure X-ray Photoelectron Spectroscopy measurements at pressures up to 30 mbar [12]. The following section gives an overview of the X-ray production at the facility as well as the treatment of the X-ray radiation at the HIPPIE beamline and finally, the experimental setup at the endstation. General settings for the experiment are discussed.

3.1. Synchrotron Light Generation for the HIPPIE Beamline

The X-ray source of the HIPPIE beamline is an elliptically polarizing undulator [12], i.e. an array of magnets that forces the electrons in the storage ring onto a slalom path. When charged particles are accelerated, which they are when changing direction, they emit radiation within a certain wavelength range. For the ultra-relativistic electrons in synchrotron light sources, this radiation is in the X-ray regime. The benefit of using undulators as insertion device instead of simple bending magnets is that the intensity of the emitted radiation can be increased by many orders of magnitude. Depending on the undulator periodicity, the gap size between the two poles, and the kinetic energy of the electrons, a specific wavelength of X-ray radiation is then produced.

The undulator for the HIPPIE beamline has 70 periods with an undulator wavelength of 53 mm. These settings enable photon production in the energy range from 250 through 2200 eV [12]. The photon fluxes reached by this source are higher than 10^{12} photons/s, making APXPS measurements possible, despite the photoelectron signal loss in the gas phase [12].

3.2. HIPPIE Beamline Optics
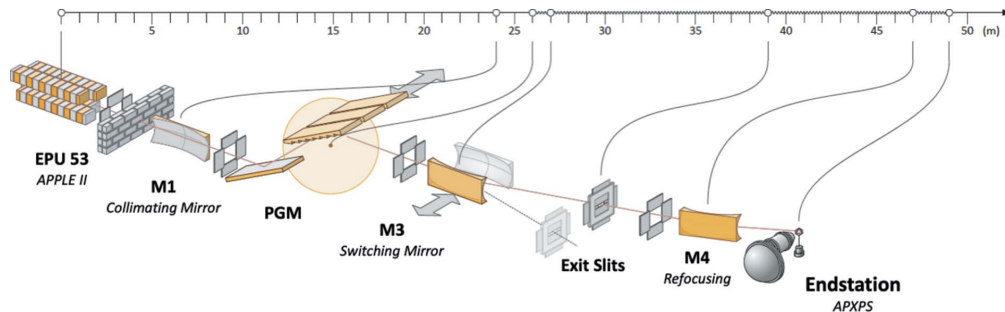
Figure 5: ***The optical instruments used at the HIPPIE beamline*** *transporting and processing the X-ray beam generated in the undulator (EPU 53). The setup contains several mirrors (M1, M3, and M4) that focus the beam, some slits, and a monochromator (PGM) where the photon energy, used at the endstation, is selected. The figure is taken from [12].*

After the X-ray beam is taken from the undulator in the storage ring, it passes through a wall to dump parts of the radiation that are not used at the endstation. Then, the beam is collimated and passed on to the plane-grating monochromator (PGM). The monochromator consists of a plane mirror (M2) and a plane grating. Subsequently, a set of baffles takes away the undesired photon energies, and a switching mirror (M3) directs the beam toward one of the two experimental branches. When entering the branch, the exit slit is adjusted to select a certain beam intensity and energy resolution of the photons in it. The beam is finally re-focused (M4) again and results in a 25 x 60 μm footprint at the sample position [12]. This results in strongly localized measurements. The photon energies that were used for the experiments of this thesis were always chosen such that the emitted photoelectrons had a kinetic energy of roughly 200 eV which is beneficial for both surface-sensitive measurements and the electron analyzer as discussed earlier.

3.3. HIPPIE endstation

The experiments in this thesis use the catalysis cell of the HIPPIE beamline. There, the analysis chamber contains a flow cell dedicated to ambient pressure (AP) measurements. In the cell, the sample is mounted on a sample holder with a hole, enabling direct sample heating with an IR laser up to 600 °C [12].

The X-ray beam is transferred into the AP chamber through a 200 nm thick silicon nitrite window [12]. When hitting the sample, the X-ray beam leads to the emission of photoelectrons that are collected by a nozzle with 0.3 mm diameter [12]. This nozzle is placed at a distance of two times its diameter from the sample surface to obtain a homogeneous pressure at the sample surface [6]. In the differential pumping stages and electrostatic lenses, the photoelectrons are transported toward the electron energy analyzer as described in the section about APXPS 2.3. A camera looking at the phosphorous screen, which visualizes the impinging photoelectrons, captures images with a maximum frame rate of 17 Hz [12].

Mass flow controllers enable a precise adjustment of the gas composition lead into the AP cell. The gases are flown from one side of the sample through the chamber and extracted at the other side of the sample. This leads to an asymmetric gas distribution within the chamber which influences the reaction above the catalyst. As we chose a constant flow through the chamber, our measurements, however, are consistent with each other.

During the experiments, the pressure within the AP cell was chosen to be approximately 5 mbar of varying gas compositions. The pressure within the cell was measured by a Pirani gauge, a capacitance manometer, and a full-range gauge [12]. All of them are placed at slightly different positions in the cell leading to different pressure values due to large pressure gradients within the cell. A QMS is installed to quickly analyze the gas composition during measurements. One possible measurement point is in the first differential pumping stage of the electron energy analyzer [12].

4. Methods

Most time-resolved spectra in this thesis are displayed in 2D image plots where the color indicates the intensity in the photoelectron spectra. To visualize this, Figure 6 A shows the 3D plot where, similar to the 2D plot, energy and time axes can be seen, but additionally also the intensity axis.
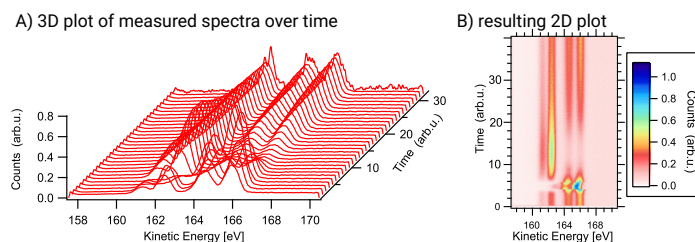
Figure 6: *A) 3D image of measured spectra over time* with one kinetic energy axis, one time axis, and one intensity axis. *B) 2D image* with time and binding energy (analog to kinetic energy) axes as in 6 A. In B, the intensity axis points out of the paper plane.

When measuring the intensity of the individual peaks in the photoelectron spectra, qualitative as well as quantitative errors exist. Before being able to analyze the data, these errors need to be corrected. The corresponding steps are shown and described in the following sections.

4.1. Normalization and Background Removal
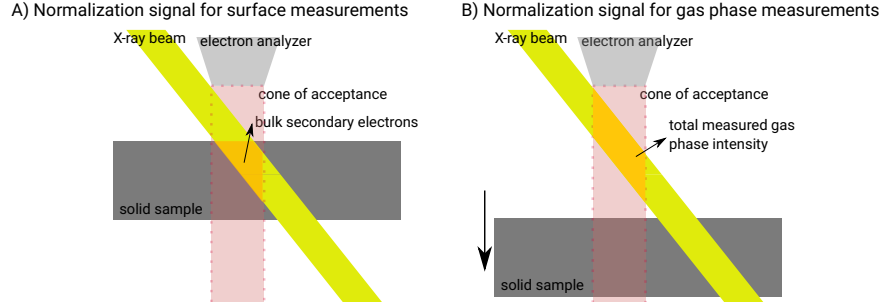
Figure 7: ***A) Normalization process for surface measurements*** *where the measured data is normalized to the background signal of secondary electrons from the bulk.* ***B) Normalization process for gas phase spectra*** *where the measured data is normalized to 1.*

Due to changes in the gas composition between the sample and the analyzer the intensity of the peaks measured in the spectra varies. To account for this, normalization of the spectrum is necessary which takes different forms depending on whether the gas phase or the surface is analyzed. This is shown in Figure 7 A, where the data for surface measurements is normalized to the signal of secondary electrons from the bulk (orange area). In Figure 7 B, the normalization for gas phase measurements is shown. Here, under the assumption that the total amount of molecules in the measurement window has to be constant, the total measured signal (orange area) is normalized to 1.

Background removal is usually only necessary for spectra measured in the vicinity of the surface of the sample as the secondary electrons from the bulk result in a continuous background. This background, however, does not provide additional information about the sample and can be removed.

4.2. Fermi Edge calibration

Referring to binding energies measured with respect to the Fermi Energy offers a possibility to compare measurements. When an electron is ejected from the sample (like electron 1 in the sketch in Figure 8), its kinetic energy is calculated by putting together the various potentials it has to travel through, as shown in Figure 8:

$$E_{\text{kin}}^{\text{Core Level}} = h\nu - \text{BE} - \Phi_{\text{sample}} \quad , \tag{6}$$

where $h\nu$ is the photon energy used to excite the electron, BE the photoelectron's binding energy in the sample, and Φ_{sample} is the work function of the sample. When this electron's kinetic energy is then measured in the analyzer, the value obtained is instead

$$\begin{aligned} E_{\text{kin}}^{\text{Core Level, Analyzer}} &= h\nu - \text{BE} - \Phi_{\text{sample}} - (\Phi_{\text{analyzer}} - \Phi_{\text{sample}}) \\ &= h\nu - \text{BE} - \Phi_{\text{analyzer}} \quad , \end{aligned} \tag{7}$$

where Φ_{analyzer} is the work function of the analyzer. When the kinetic energy of electrons at the Fermi edge is measured their binding energy is per definition zero. Therefore, it is

$$E_{\text{kin}}^{\text{Fermi edge, Analyzer}} = h\nu - \Phi_{\text{analyzer}} \quad . \tag{8}$$

Thus, the kinetic energy of these electrons is the highest energy measured in the detector, ideally, there should be no electron energies measured above this.

In reality, though, the onset of the signal around zero binding energy is not sharp. It is rather a slightly extended step over a few eV, especially if there is a non-conductive layer on top of the sample. That extension can be observed in Figure 9. To still be able to determine a value for the Fermi energy, a convolution between a fermi-dirac function and a step function is fitted to the edge data. Determining the kinetic energy where the edge has the largest slope, yields the Fermi Energy. This process is shown in Figure 9. When subtracting the kinetic energy of a core-level electron from the one of an electron at the Fermi edge, an expression for the binding energy of the core-level electron remains independent of the sample or analyzer work functions:

Figure 8: *Electric potentials along the chamber geometry together with a core level of the sample and two electrons passing through the potential landscape.*

$$\text{BE} = E_{\text{kin}}^{\text{Fermi edge, Analyzer}} - E_{\text{kin}}^{\text{Core Level, Analyzer}} \quad . \tag{9}$$

It is, thus, a value that is comparable throughout various experimental setups. Furthermore, it is insensitive to the photon energy used. This monochromatic energy is selected by adjusting mirrors in the beamline. However, there is always a small error in the X-ray energy due to mechanical adjustment of the mirrors. This error is now not affecting the retrieved binding energy anymore, as the photon energy is removed from the expression.

If, then, an electron is ejected from a gas phase molecule (like electron 2 in Figure 8), its kinetic energy is just

$$E_{\text{kin}}^{\text{gas}} = h\nu - \text{BE} \tag{10}$$

as it does not need to overcome the sample work function. The kinetic energy measured in the analyzer is

$$\begin{aligned} E_{\text{kin}}^{\text{gas, Analyzer}} &= h\nu - \text{BE} - (\Phi_{\text{analyzer}} - \Phi_{\text{sample}}) \\ &= h\nu - \text{BE} - \Phi_{\text{analyzer}} + \Phi_{\text{sample}} \quad . \end{aligned} \tag{11}$$

Together with the kinetic energy of the Fermi edge electrons, this gives

Figure 9: *Measured data around the Fermi edge together with the fitted curve, giving the real Fermi energy.*

$$\text{BE} - \Phi_{\text{sample}} = E_{\text{kin}}^{\text{Fermi edge, Analyzer}} - E_{\text{kin}}^{\text{gas, Analyzer}} \quad . \tag{12}$$

17

There, not the binding energy of the electron is obtained but the so-called *apparent binding energy*. This includes the work function of the sample, which leads to the effect that the apparent binding energy of gas phase electrons changes when the sample surface phase, and hence Φ_{sample}, changes.

4.3. Fitting Process

After the measured spectra are corrected in all the aforementioned respects and before the actual fitting process takes place, the axes of the spectra are rescaled to fit certain criteria. In order to compare measurements conducted with different setups, the binding energy scale is used. Observing periodic changes in the spectrum due to the applied temperature ramps to the sample, the time for one such period is known. This can then be used to calibrate the time axis of the 2D image.

That image then contains the data that is prepared to be fitted to mathematical functions. These are so-called Voigt Functions, a convolution of a Lorentzian function accounting for peak broadening due to the lifetime effects of the core hole created by photoemission, and a Gaussian function. The latter describes the peak broadening due to instrumentation. The fit adapts the coefficients in the sum of several Voigt Functions so that they fit the measured data the best. The coefficients that are adjusted, are the intensity as well as the binding energy, and lastly the Gaussian width of every peak. During fitting, the parameters are constrained to be positive values. This process can be seen in the figures during the discussion of the experimental results. To obtain an ideally tailored analysis tool, the scripts for this have been written as a part of this thesis and are partly shown in the appendix.

Making the fit more performing, some Voigt coefficients are set to be constant, for example, the Lorentzian width of the peaks which is forced to be 0.1 eV [16], and the offset which is set to zero. When starting a fit over the whole acquired 2D image, every single spectrum is fitted individually. Here, in the first few spectra, all coefficients are free to vary. Later, restrictions on peak intensities are implemented if applicable. This is for instance the case for the oxygen double peak. A core hole can be filled by two different electrons leading to two different final states that result in a peak splitting. According to the theory, this leads to a 1:2 ratio in the peak intensities. In practice, this ratio deviates a bit from that value but it is fixed. That ratio is then determined in the first few fits and later on kept constant. The binding energies of the peaks are only allowed to vary within a small, previously manually determined, range. This is done to avoid interruptions of the fit, e.g. when the peak intensity approaches zero, but to still allow work function shifts for gas phase spectra. The fit code was written in IGOR 8.0.4.2, a scientific data analysis software provided by WaveMetrics Inc. Overall, the code fitted up to 12 free parameters per spectrum with over 15,000 spectra per measured region.

When analyzing the spectra, the error analysis usually concerns the peak position, the peak width as well as its intensity, all of their errors are provided by the fit function used. In this case, however, many spectra are measured which makes such an error analysis very time-consuming. A more useful way to estimate errors is by using the signal-to-noise ratio in the data obtained from fitting the whole 2D spectrum.

5.   Methane oxidation over thick Pd oxide surface phases

During the first set of experiments, the polycrystalline Pd catalyst was placed in gas flow settings of 1.65 sccm (standard cubic centimeters per minute) oxygen and 1.5 sccm methane which lead to a gas pressure of 3.8 mbar above the catalyst surface. Thus, at a temperature of 20 °C $1.5 \times \frac{1000}{3.8}$ ml methane are injected into the chamber per minute. The temperature ramps were chosen as shown in the lower panel of Figure 10, to enforce surface oscillations between a thin and a thick Pd oxide. The temperature profile, hence, is programmed, so that the catalyst temperature is ramped between 350 °C and 585 °C, each of which is maintained for 35 s. The heating rate is chosen to be 11 °C/s.

The upper panel of Figure 10 displays the gas composition probed by a QMS through the nozzle of the electron analyzer. It can be observed, that the application of temperature ramps to the Pd sample has effects on the gas phase composition above the catalyst surface. For instance, the reactant concentrations, i.e. oxygen (O_2) and methane (CH_4), oscillate in an opposite fashion to the product concentrations, i.e. carbon dioxide (CO_2), and carbon monoxide (CO). The water signal behaves differently which is commented on further in the discussion of this section.
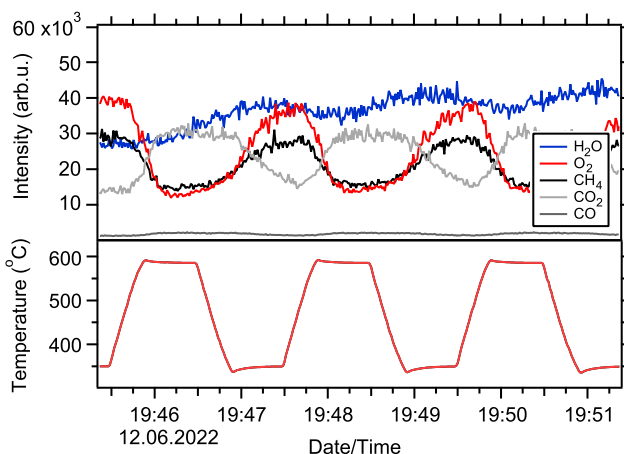
Figure 10: ***QMS data*** *following a temperature train like the one shown in the lower panel, i.e. the temperature applied to the catalyst follows a ramp train that repeats 585 °C (60 s) - 350 °C (60 s). All gas phase components are visible, showing clear effects of the applied temperature.*

The following section discusses the tr-APXPS data obtained while ramping the temperature as shown in Figure 10. Both, the O 1s and the C 1s gas phase spectra have been measured subsequently, as well as the C 1s, O 1s, and Pd 3d surface spectra. An effect of the increasingly thick oxide layer is that the Fermi edge is not measurable anymore. Therefore, these data have been calibrated using the Fermi edge data of the previous data set for the respective photon energies.

5.1. Gas Phase Spectra
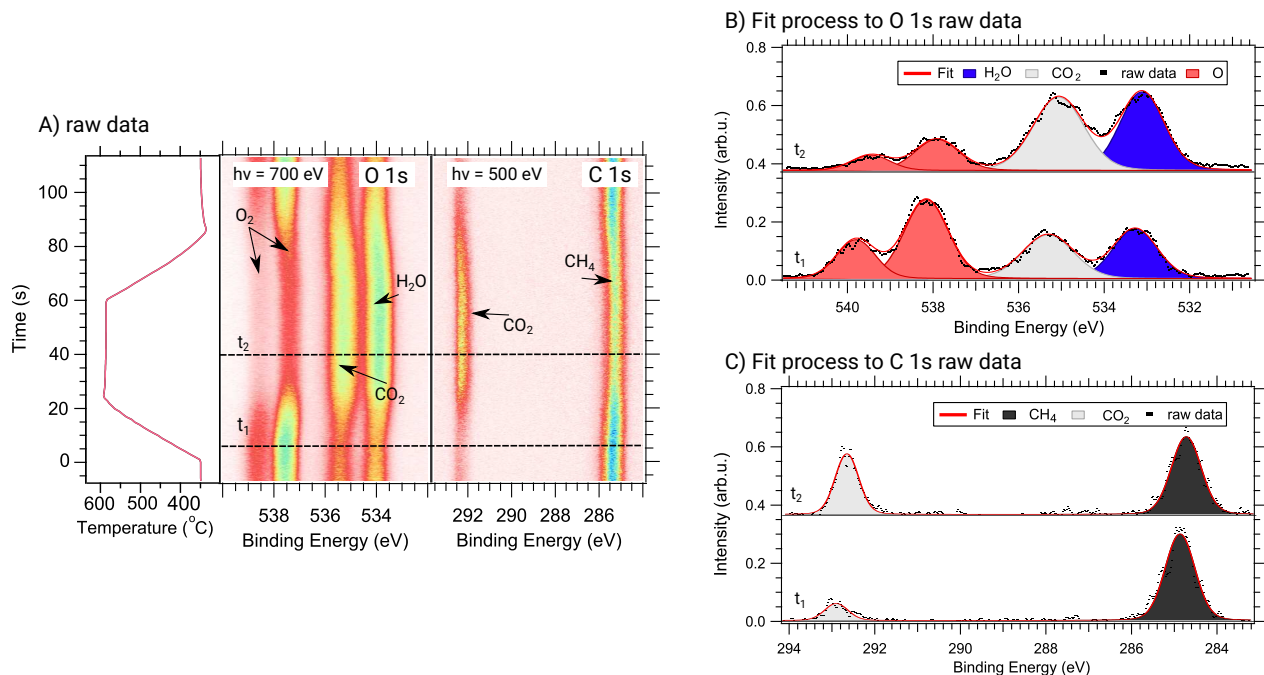
Figure 11: *A) Measured raw data*, *i.e., the temperature of the catalyst, O 1s, and C 1s gas phase spectra, after the respective corrections to the spectra.* ***B) Example of fit to the O 1s spectra*** *and* ***C) Example of fit to the C 1s spectra*** *for two different times, displaying the individual molecular contributions.*

Figure 11 A shows the treated O 1s and C 1s gas phase spectra together with the catalyst temperature. Panels B and C show two examples of curve-fitting of Voigt functions at the times t_1 and t_2 as indicated in Panel A. The O 1s and C 1s spectra were time-aligned using the development of the CO_2 component. The time stamp zero was chosen as the start of the temperature ramp.

The observable peaks in Panel B are a water component at 533.8 eV / 534.1 eV (blue in the later discussion), a CO_2 component at 535.2 eV / 535.5 eV (light grey), and an oxygen double peak component resulting from two different final states of the photoemission process at the binding energies 537.3 eV / 537.6 eV and 538.4 / 538.7 eV, respectively (red). In Panel C, the observable components are CH_4 at an apparent binding energy of 285.2 eV / 285.5 eV (black) and CO_2 located at 292.2 eV / 292.5 eV (light grey).

The peak intensities obtained from the fitting process to all spectra in Panel A of Figure 11 were transformed into partial pressures by accounting for the number of equal atoms in each molecule and assuming a constant chamber pressure. For instance, I divided the obtained CO_2 intensity in the O 1s spectrum by two as there are two oxygen atoms probed in a carbon dioxide molecule. The resulting partial pressures are displayed in Figure 12 A. The lower part of that panel shows the development of the apparent binding energies of CO_2 (left axis) and H_2O (right axis). The other gas phase components which are not shown there exhibit the

same behavior. Additionally, the respective extract of the temperature profile is displayed. In Panel B, the water and oxygen partial pressure developments, from Panel A, are plotted against the catalyst temperature. All of these results correspond to the gas phase in the close vicinity of the surface.
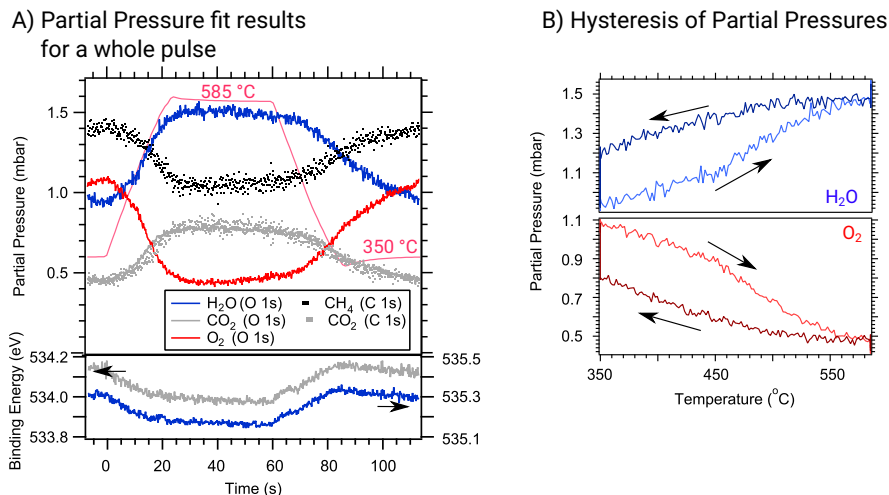
Figure 12: *A) Fit results for a whole temperature ramp* *including the development of partial pressures and the binding energies are shown, taken from the fitting process shown in Figure 11. The respective part of the temperature ramp is shown in antique pink to relate the developments to the catalyst's temperature.* *B) Exemplary hysteresis of the oxygen and water partial pressures* *with respect to the catalyst temperature.*

When discussing the features independent of the time development within this experiment, the following two observations can be made. First, the reaction is not mass transfer limited, i.e. the observed oxygen and methane signals are always larger than zero as Figure 12 A demonstrates. Hence, no partial combustion is expected which agrees with the fact, that no CO signal is observed in either the O 1s or the C 1s spectra in Figure 11.

Secondly, I focus on the reaction pathway for methane processing. For complete combustion,

$$CH_4 + 2\,O_2 \longrightarrow CO_2 + 2\,H_2O, \tag{13}$$
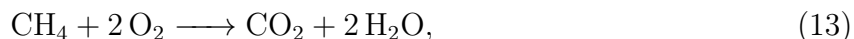
a 2:1 ratio is expected for the water and carbon dioxide signals. As introduced earlier in 2.4, every methane molecule combusted results in $2\,H_2O$ molecules. Thus, if partial combustion or carbon deposition were happening additionally, the H_2O to CO_2 ratio would be higher. When inspecting the pressure signals displayed in Figure 12 A, the water pressure is, indeed, twice as large as the carbon dioxide pressure during the whole ramp. Thus, all methane is combusted completely within this experiment.

When looking at the most drastic changes in the time evolution of the partial pressures, it is observed that these happen when changing the catalyst temperature. In the display of partial pressure in Panel A, it can be seen, that the conversion rate closely follows the temperature ramp applied to the catalyst when ramping up the temperature. That means, that the conversion rate quickly starts to rise when the temperature increases, which is in

agreement with the Arrhenius equation 1. When the temperature drops again, the conversion rate follows only slowly, suggesting hysteresis in this system. To explicitly show this, Panel B plots the partial pressure of water and oxygen against the temperature of the catalyst. There, a pronounced hysteresis is observed which will be explainable when discussing the surface spectra.

Now, the time evolution during constant catalyst temperatures can be discussed. Analyzing closely first the development of partial pressures in Panel A, weak changes in the gas phase signal can be observed when keeping the catalyst at a constant temperature, e.g. 585 °C. That is, the pressure of the CO_2 and H_2O signals increases slightly whereas the product pressures decrease. That suggests a changing methane conversion rate which, in turn, indicates a gradually changing surface phase.

When looking at the development of apparent binding energies in 12 A, it can be seen that both apparent binding energies shown shift in the same way even though the fitting process did not assume this. A changing work function, thus, a changing surface phase is responsible. Therefore, at constant temperatures, gradual changes in the surface phase are expected while more extreme changes are present when ramping the temperature. This supports the observations made when discussing the partial pressures.

Concluding the findings from the gas phase, the most important result is that no shortage of the reactants is observed, leading to the continuous complete combustion of methane. Additionally, constant changes in the surface phase are expected, more radical when ramping the temperature and more gradual when keeping the catalyst's temperature constant. Finally, it can be stated that a hysteresis of the conversion rate is observed when following the temperature ramp.

5.2. Surface Spectra
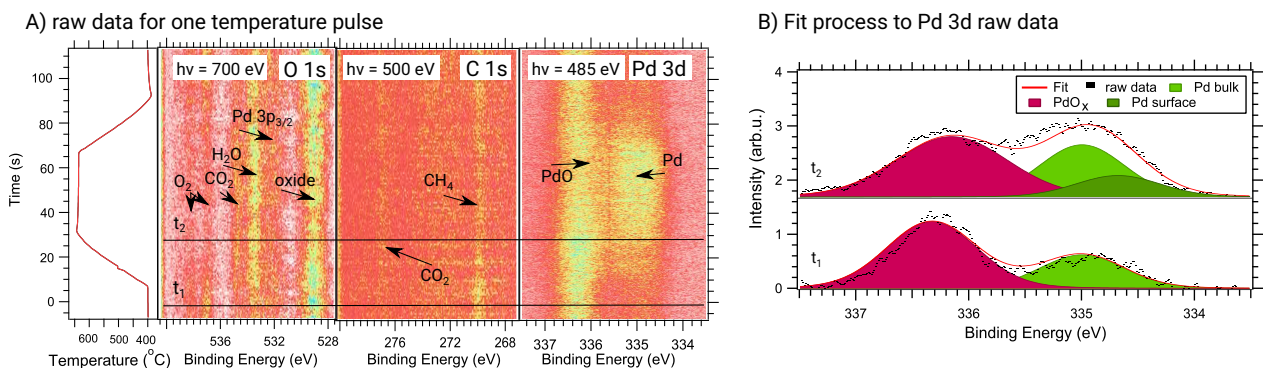
Figure 13: **A) Measured raw data**, *i.e., the temperature of the catalyst, O 1s, C 1s, and Pd 3d surface spectra for one temperature ramp, after the respective corrections to the spectra.* **B) Example of fit to the Pd 3d spectra** *for two different times, displaying the individual molecular contributions.*

Figure 13 A shows the treated O 1s, C 1s, and Pd 3d spectra. Panel B shows two examples of curve-fitting at the times t_1 and t_2 as indicated in Panel A. The C 1s data is not fitted as it

22

does not contain any surface components. The only visible components are the CH_4 and CO_2 gas phase signals. Also, the O 1s data is not treated further due to the low signal-to-noise ratio (see appendix for further discussion of this). In the Pd 3d spectra, two large peaks are visible. Due to the variety of expected oxide components and, thus, a complicated fitting process, a three-component system was chosen. The broad peak at lower binding energies contains contributions of a Pd bulk signal at 335.0 eV (grass green) as well as a Pd surface signal at 334.6 eV (dark green). These values are kept fixed during the fitting process and are based on the results in [17] and [18]. The other broad peak appears due to various oxide species and is fitted with a flexible binding energy (wine red).

The results of the fitting process to the raw data are displayed in Figure 14. The original fitted data are displayed by markers while the solid lines are a smoothed representation of that data and serve as a guide to the eye. The respective part of the temperature ramp is included in the figure to relate the changes on the surface to the temperature of the catalyst.
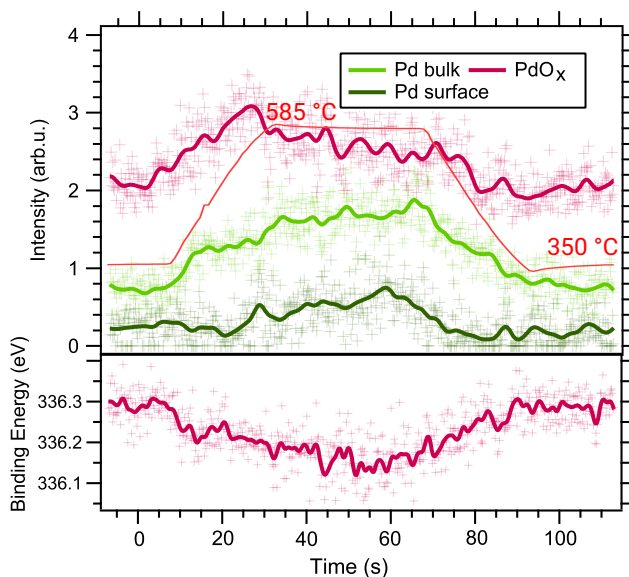
Figure 14: *Pd 3d fit results where the more solid lines serve as a guide to the eye in the noisy data. Additionally, the respective extract of the temperature ramp is shown to relate the surface phase to the temperature of the catalyst.*

The first observation that can be made when discussing the intensity development in Figure 14, is that the surface oscillates back and forth between a thick and a thin oxide. The information about the thickness is taken from the intensity of the Pd bulk signal. As more Pd bulk is measured during high catalyst temperatures, the oxide must be thinner, assuming an approximately constant probing depth into the catalyst. Additionally, there is some evidence for a metallic surface signal, though this is certainly a minority phase. When looking at the ratio between the Pd bulk signal and the oxide component, it is approximately 1:1 when the catalyst is kept at high temperatures. That is a significantly higher ratio than found by Fernandes *et al.* in [17] for a monolayer oxide. Additionally, the literature data was measured with a photon energy of 400 eV, therefore, the measurements were slightly more

surface sensitive. Thus, this data suggests, that the thin oxide in this study is still a few monolayers thick.

In the lower panel of Figure 14, a gradual changing binding energy of the oxide component within this simplified model is observed being evidence of a change in the surface oxide phase. This, however, cannot be related to a clear surface oxide due to the polycrystalline nature of the Pd sample, i.e. various surface orientations are exposed to the gas phase, resulting in the formation of different oxide phases. It can, however, be said that the oxide phase at low temperatures is different from the one at high temperatures, judging by the low and high binding energy.

When relating these findings, i.e. the existence of different oxide phases, to the temperature of the catalyst, it becomes evident that, for a catalyst temperature of 585 °C, the thin oxide is more prominent, while the thick oxide grows for lower temperatures, i.e. 350 °C. When the temperature has reached the constant temperature of 585 °C or 350 °C, respectively, continuous, gradual changes in the thickness of the oxide phase are observed, again judging by the observed Pd bulk signal. The existence of these surface oxides can be related to the hysteresis in the conversion rate observed in Figure 12 B. As the response of the conversion rate to temperature changes is obviously different for the different oxides and the transitions between them, the hysteresis is suggested to be caused by different growing speeds of these oxide phases as observed for instance in [19].

Summarizing these findings, it needs to be mentioned first and foremost that the Pd catalyst surface oscillates back and forth between a thick PdO phase and a thinner one. Furthermore, it can be seen that the buildup of a thick oxide takes some time, while the formation of a thin oxide happens rather quickly.

5.3. Discussion
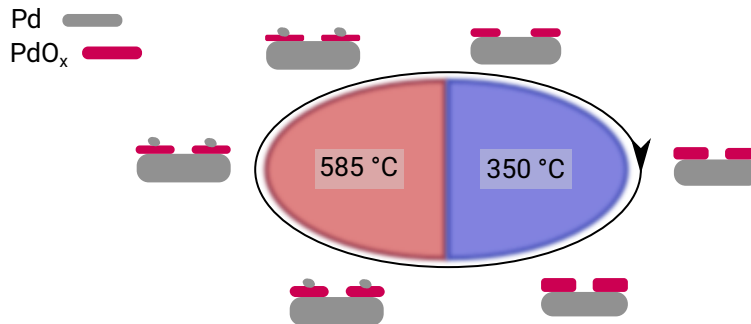
Figure 15: *Schematic of the proposed surface phase development* during the application of 585 °C (60 s) - 350 °C (60 s) temperature ramps as shown in Figure 10.

Using the knowledge acquired from the tr-APXPS spectra discussed here, a scenario for surface changes can be presented. For that, the oxide reduction mechanism suggested by Goodwin *et al.* in [20] was used. It proposes that metallic Pd islands form on top of the oxide when the oxide thickness decreases.

24

First, when heating the catalyst up to a temperature of 585 °C, the conversion rate increases. This is most likely a temperature-driven effect. Furthermore, the thickness of the oxide decreases as the catalyst's temperature is above the decomposition temperature for PdO_x [19]. The chemical effect, that dissociated methane reacts with the surface oxide forming water and carbon dioxide, is most likely less dominant. Thus, the thermal reduction leads to a thinner oxide phase. This changing surface phase was already indicated by the changes in the work function shift, observed in the apparent binding energy of the gas phase components, as well as the changing binding energy of the PdO_x component. When the catalyst is then kept at the high temperature, the thickness of the oxide is decreased further, leading to an overall decreasing conversion rate. Once the temperature drops to 350 °C, the conversion rate decreases, and more oxygen is available for building up a thick oxide. When the catalyst temperature is then kept constant, this process continues albeit slower.

Finally, when comparing the results obtained from the QMS, presented at the beginning of this section, and the tr-APXPS measurements, it is especially obvious in the water signal that the QMS provides false information. Concerning the exact development of the other components, one needs to pay attention to the fact that the QMS probes the gas composition 6 mm above the surface, as schematically shown in the theory section about APXPS 2.3. The composition there can only be seen as an average of the gas composition in the entire experimental cell, hence, local deviations cannot be probed. This is especially relevant since Zetterberg *et al.* [21] showed that the gas composition within the cell is not homogeneous, using Planar Laser-Induced Fluorescence. Furthermore, the water signal measured with the QMS is smeared out as, due to the adsorption of H_2O molecules to the chamber walls, their desorption and thus the measurement happens at an arbitrary time.

To summarize, the system presented in this study is characterized by surface oxides of varying kinds that are present throughout the whole temperature cycle. Furthermore, a quickly evolving thin oxide surface phase is observed, while the formation of the thick PdO phase is rather slow. Finally, and most importantly, whichever oxide is present at the surface, methane is only processed via complete combustion within this experimental system.

6. Methane oxidation over thin Pd oxide, carbide and metallic surface phases

In contrast to the previous experiment, where no reaction reactant was in short supply, the conditions within this experiment were chosen in such a way that the reaction is partly limited by the oxygen supply. Thus, the gas composition in the AP cell was chosen to be 3.5:0.5 sccm CH_4:O_2, i.e. highly methane-rich, at a total pressure within the cell of 5.3 mbar. The temperature ramps were programmed to be exactly like in the example in the lower panel of Figure 16, i.e. the laser was programmed to heat up the polycrystalline Pd sample with a constant heating rate of 5 °C/s from 450 °C to 525 °C. After 30 s of first ramping and then dwelling at 525 °C, it was aimed for 350 °C, and, another 60 s later, the new temperature was set to be 450 °C . Then, again including the heating ramp, the catalyst was kept at 450 °C for 900 s until a new ramp began.

Again, during the measurements, the gas phase composition was simultaneously measured

with a QMS, some results are presented in Figure 16 together with the respective temperature of the catalyst. The effect of the temperature ramps is clearly visible in the conversion rate represented by reactant and product concentrations. Again, the weak modulation of the water signal can be observed, which, as is known from the previous study, will be better observable in the tr-APXPS spectra. In contrast to the previous study, however, it can be observed here, that the oxygen signal drops to zero, indicating measurements in the O-MTL.
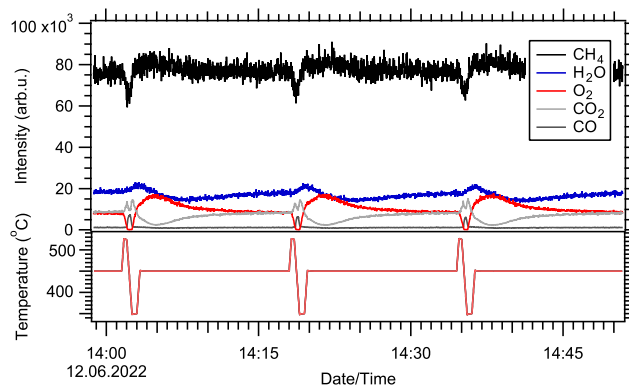
Figure 16: *QMS data following a temperature train like the one shown in the panel below. All gas phase components are visible, but measured centimeters away from the surface, thus, no direct conclusion of the local surface activity can be drawn.*

6.1. Gas Phase Spectra
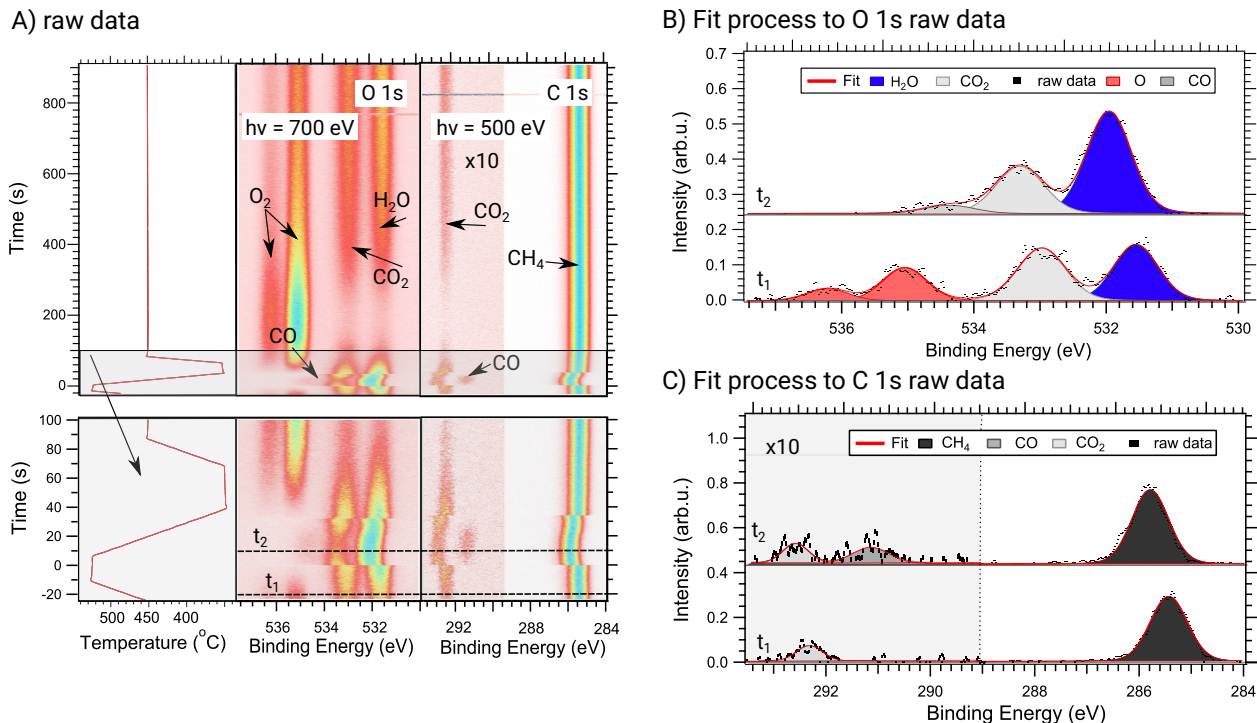
Figure 17: **A) Measured raw data**, *i.e., the temperature of the catalyst, O 1s, and C 1s gas phase spectra, after the respective corrections to the spectra. The left side of the C 1s spectra is multiplied by a factor of 10 for better visibility of the light components.* **B) Example of fit to the O 1s spectra** *and* **C) Example of fit to the C 1s spectra** *for two different times, displaying the individual molecular contributions.*

Probing directly above the surface, the tr-APXPS data were measured and are shown in Figure 17 A. Panels B and C show examples of the fitting at two times, t_1 and t_2, as indicated in Panel A. To time-align the O 1s and C 1s spectra, the absolute time where the shift of the sample's work function, visible in the apparent binding energies, occurs, was set to be zero.

The peaks observed in Panel B are identified as H_2O at 531.6 eV / 532.0 eV (blue) (t_1/t_2), CO_2 at 533.0 eV / 533.4 eV (light grey), CO at 534.5 eV (only observable at t_2, dark grey), and an O_2 double peak at 535.1 eV and 536.2 eV, respectively (red). The oxygen contribution is only visible at t_1. In Panel C, the strong component at 285.4 eV / 285.8 eV (black), is assigned to methane. Also, two weak signals, where higher contrast was needed to make them visible (these signals together with the surrounding were multiplied by a factor 10), can be seen. One is identified as a CO at 291.3 eV (only measurable at t_2, dark grey), and the other one as CO_2 at 292.3 eV / 292.7 eV (light grey).

Analog to the process in the previous section, the fit results to the data in Figure 17 A are presented in Figure 18. There, Panel A shows the respective developments for an entire temperature ramp, while Panel B focuses on an extract of the ramp where the most

rapid changes in pressure occur. As for the development of partial pressures, the methane component refers to the scale of the right-hand axis while the others are accounted for by the left one. This is done to better visualize changes in the respective partial pressures as the methane signal is much more intense. For comparison purposes, the extracted temperature ramp is additionally plotted in the extracted partial pressure plot.
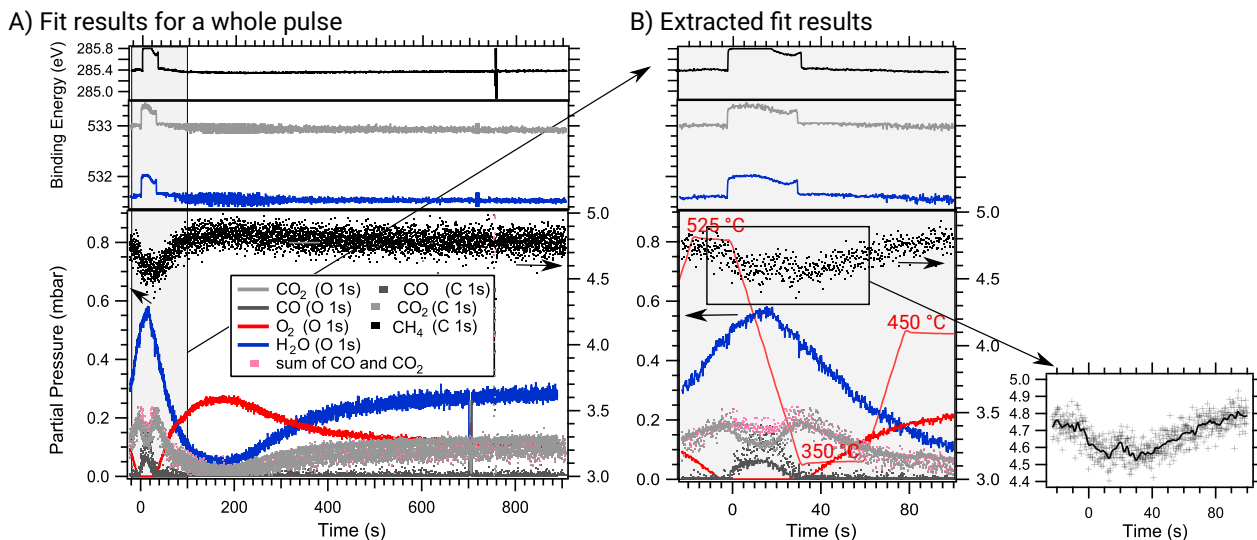
Figure 18: *A) Fit results for a whole temperature ramp and B) Fit results for an extracted time region* are shown. The catalyst temperature is shown in antique pink. In the partial pressure development, the methane component is accounted for by the right-hand axis while the other components refer to the left one.

Because the catalyst, here, is placed in an oxygen-lean environment, the conversion rate is either limited by the amount of available oxygen or the surface activity. The inspection of the lower panels in Figure 18 clearly shows that, at the beginning of a temperature ramp, i.e. at 450 °C, both an O_2 and a CH_4 signal are observable. Therefore, the reaction was limited by the catalyst activity at the beginning of the temperature ramp. Subsequently, when the temperature has been at 525 °C and starts dropping to 350 °C, the O_2 pressure above the surface drops to zero. The reaction is now in the MTL of oxygen. Later, at t = 30 s, the reaction exits the O-MTL and the conversion rate is limited by the surface activity again. This measurement in the O-MTL is, therefore, in contrast to the previously discussed study where the conversion rate was limited by the surface activity throughout the whole measurement.

When looking at the apparent binding energy development of the three most intense and least noisy signals, i.e. CH_4, H_2O, and CO_2 in Panel B, observations can be made that strongly indicate changing surface phases. At the entry into the oxygen MTL, a common, sudden jump in all apparent binding energies, i.e. due to a changed work function, is observed which is evidence for an almost instantaneous appearance of another surface phase. Within the O-MTL, a slight decrease of 0.1 eV in the work function at t ≈ 15 s, due to a gradually changing surface is followed by a drop at the end of the O-MTL, reaching the initial apparent

binding energy again. Therefore, the surface phase before and after the oxygen MTL might be similar.

An important conclusion that can be drawn from the inspection of the development of partial pressures in Panel B, is related to the fact that a CO signal is only observed during the oxygen MTL, i.e. between t = 0 and t = 30 s. That means that only the short supply of oxygen in the vicinity of the surface leads to carbon monoxide formation.

The analysis of the partial pressures in Panel B leads to a second pronounced observation. First, before the reaction is entering the MTL of oxygen, i.e. at t < 0, both, an oxygen signal and a methane signal are measured, and, thus, complete combustion is expected. According to the reaction equation

$$CH_4 + 2\,O_2 \longrightarrow CO_2 + 2\,H_2O, \tag{14}$$
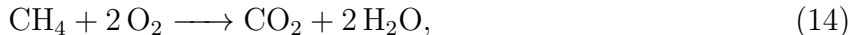
that would result in double the increase in the H_2O pressure compared with the CO_2 pressure, when more methane is combusted. In the Figure, however, it can be observed that the slopes of the increasing CO_2 (0.002 mbar/s) and H_2O (0.010 mbar/s) pressures vary more than by a factor two (see appendix for the fits). Additionally, in the O-MTL, i.e. at 0 < t < 30 s, the sum of the CO and CO_2 signals (pink dots) decreases while the water signal increases which is clear evidence for another reaction pathway being present. Finally, the deviations between the water signal and the sum of CO_2 and CO gradually become less when exiting the O-MTL and decrease more and more with advancing time. These indications lead to the conclusion, that a reaction must be taking place where the products are water and another molecule that cannot be observed within these gas phase spectra.

A closer look into the development of partial pressures shows a drop of the conversion rate approximately in the middle of the oxygen MTL at t = 15 s, indicated by decreasing water pressures. This rather sharp change happens simultaneously with the slight drop in apparent binding energy, resulting from a changing surface phase, which might be an explanation for the reduced conversion rate. It could, however, also be coincided with the dropping temperature of the catalyst. It is puzzling though, that, in the meantime, the methane signal first increases, indicating a lower conversion rate, but then decreases again, as can be seen more clearly in the extract of the methane development.

Looking into the development of partial pressures now in Panel A, continuing along the time axis, at t ≈ 200 s, the reactant signals, i.e. O_2 and CH_4, reach a peak while the product signals experience their lowest pressures. Later, the conversion rate seems to gradually increase again. All this happens, quite surprisingly, at a constant catalyst temperature which indicates that the effects are solely caused by a changing surface phase.

To summarize, the most important results obtained from the O 1s and C 1s gas phase spectra are first and foremost that one additional reaction, most likely carbon deposition, must take place in addition to complete and partial combustion under these reaction conditions. Furthermore, in the middle of the O-MTL, a falling instead of a previously rising conversion rate is observed. It is unclear at this point, however, whether that effect is surface or temperature-induced. Finally, at t ≈ 200 s, a surface phase is suggested to develop that results in a very low conversion rate. These findings will now be further discussed when analyzing the C 1s, O 1s, and Pd 3d surface spectra.

6.2. Surface Spectra
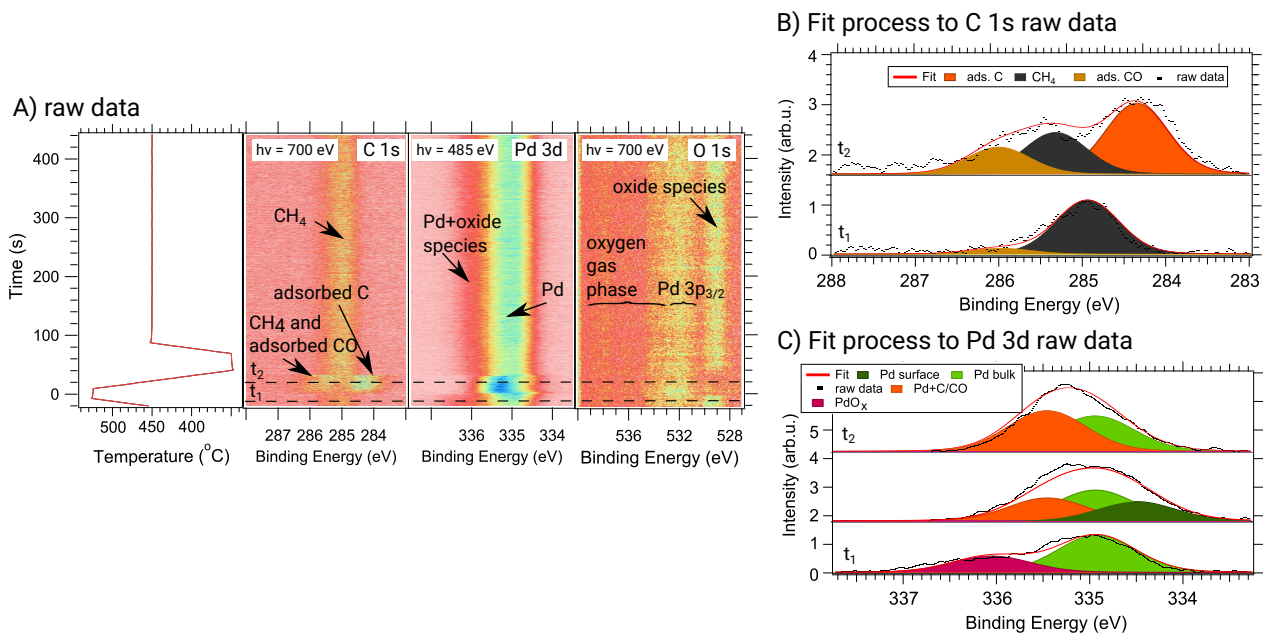
Figure 19: *A) Measured raw data*, *i.e., the temperature of the catalyst, C 1s, Pd 3d, and O 1s surface spectra, after the respective corrections to the spectra discussed in the method section.* **B) Example of fit to the C 1s spectra** *and* **C) Example of fit to the Pd 3d spectra**, *displaying the individual molecular contributions.*

In Figure 19 A, the C 1s, Pd 3d and O 1s spectra are shown together with the catalyst temperature. Panels B and C show examples of the fitting of Voigt functions to the measured spectra (which have been binned 25 times in the time-direction for better visibility) at two times, t_1 and t_2, as indicated in Panel A. Panel C additionally shows one intermediate spectrum at the surface phase shift.

In the C 1s spectra in Panel B, three components are observed. As surface APXPS spectra also include gas phase components, and since it is known from the previously discussed gas phase spectra and the QMS data that methane is by far the most intense gas phase component, a CH_4 signal is expected here. Thus, the component at an apparent binding energy of 285.1 eV (black) is assigned to methane in agreement with the results in the gas phase discussion. At the conditions within the O-MTL, also a component of adsorbed CO is expected at the surface which is fitted at 286 eV (brown), based on the results for adsorbed CO on Pd(100) [18]. Finally, the component at a binding energy of 284.4 eV (orange) is assigned to atomic carbon on the surface. This fits together nicely with the value of 284.3 eV reported in the literature [22].

Discussing the Pd 3d spectra in Panel C, a Pd surface component, a Pd bulk contribution, some Pd carbide peak as well as Pd components bound to adsorbed CO, and to surface oxygen are expected. As the component for surface Pd binding to CO (335.5 eV) and to carbon (335.4 eV) are expected at almost identical binding energies, they are fitted by one

30

component at 335.45 eV (orange). The Pd surface contribution is fitted using a fixed binding energy of 334.6 eV (dark green), while the Pd bulk component was fitted by a component at 335.0 eV (grass green). Finally, the Pd component assigned to various oxide phases is fitted at 336 eV (wine red). These values are based on the findings in [17] and [18].

Even after significant binning, it is not possible to achieve a sufficiently high signal-to-noise ratio for the fit results of the O 1s spectra (further discussion in the appendix). Thus, the following discussion only focuses on the major developments within the tr-APXPS data.

The alignment of the time axis of the C 1s and Pd 3d data was done by first setting the absolute time of the methane work function shift to zero. Then, the falling edge within the adsorbed C development, observed in the Pd 3d and the C 1s spectra, has been aligned. The fit results to the raw data in Figure 19 A are presented in Figure 20 A and B while Panel C combines those two developments. The Pd 3d intensity developments are shown for a whole temperature ramp while the C 1s intensity development focuses on the area with the most drastic changes.
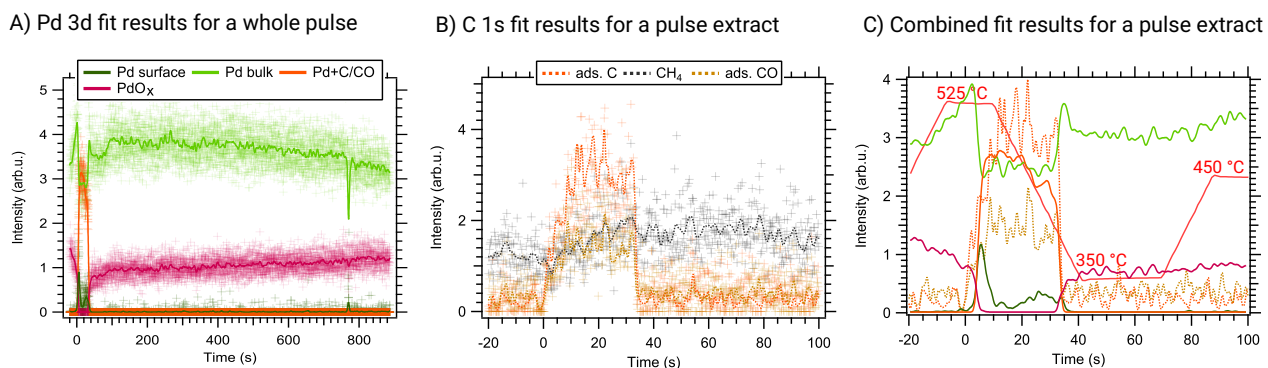
Figure 20: *A) Pd 3d intensity fit results for a whole temperature ramp and B) C 1s intensity development for a shorter time frame are shown. The solid lines in A and B are a guide to the eye within the noisy data. C) Collocation of the fit results for the C 1s and Pd 3d surface spectra where only the solid lines are shown for better visibility. The respective part of the catalyst temperature ramp is shown.*

When looking at the intensity development of the Pd 3d components in Figure 20 C, it becomes visible that the vanishing of the oxide and the emergence of the carbide is accompanied by the short existence of a metallic surface (this can be seen in more detail in the appendix). During the whole O-MTL, a carbon component is detected on the surface.

Another observation can be made in Panel C when following the components of adsorbed carbon and adsorbed CO. Both, the Pd 3d and the C 1s spectra, show a sharp increase in these components at t = 0, i.e. when entering into the O-MTL, as well as a sharp drop when exiting the O-MTL at t ≈ 30 s. The behavior of these components within the O-MTL, however, differs slightly when comparing the Pd 3d and the C 1s fit results, even though the signal-to-noise ratio is high. The observed deviation is that, while the components maintain a more or less constant intensity during the whole O-MTL in the C 1s data, the Pd 3d data show a weak decrease in intensity starting at t ≈ 20 s. As only a little oxygen is available, this decrease in the carbon coverage cannot solely be explained by the reaction between oxygen

and adsorbed carbon, thus, a likely scenario is carbon segregation into the bulk. That is reasonable since carbon, at higher temperatures prefers to stay at the surface of a material, and, reaching lower temperatures is more likely to be found in the bulk of the material [23, 24]. Thus, in the middle of the O-MTL, a temperature might be reached where segregation from subsurface layers into the bulk starts. This hypothesis is also supported by the carbon signal in the more bulk-sensitive C 1s spectra (due to a higher photoelectron kinetic energy). Here, the adsorbed C signal increases with a smaller slope than in the Pd 3d fit results, indicating that the several probed atomic layers are only gradually filled up with carbon. Toward the end of the O-MTL, the intensity of adsorbed carbon decreases again, indicating, that also the subsurface layers are gradually vacated by carbon again.

Focusing on the major developments in the O 1s data in 19 A, the averages over some spectra before, within, and after the O-MTL are compared in Figure 21. It can be observed that the peak containing the oxide components is more intense at higher binding energies before the O-MTL (green) and more intense at lower binding energies once exiting the O-MTL (blue), as visualized by the red, dashed lines. The slight shift in binding energy indicates the presence of slightly different surface oxides. Overall, however, the oxide coverage before the O-MTL is higher than after the O-MTL, proving that the surface oxide grows when the catalyst is kept at a constant temperature of 450 °C. This is also observed in the Pd 3d fit results in Figure 20 A, where the oxide component grows stronger over time while the Pd bulk component weakens.
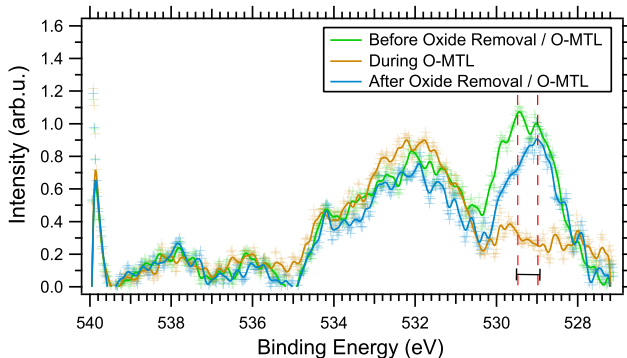
Figure 21: *Comparison of the average over some O 1s spectra before, in, and after the O-MTL* displaying a binding energy shift in the peak containing surface oxide components. During the O-MTL, no pronounced oxide is observed.

The observations made discussing the surface spectra can then be related to the ones from the discussion of the gas phase spectra. The increasing conversion rate in the first half of the O-MTL, evident by the reduced CH_4 partial pressure in Figure 18 B, happens due to the opening up of two additional reaction pathways, i.e. partial combustion of methane and carbon deposition. As atomic carbon is continuously deposited on the surface, methane is removed very efficiently from the gas phase. The slight drop in the apparent binding energy of the gas phase components in the middle of the O-MTL, due to a changing work function of the sample, is evidence of a changing surface phase. As no changes are observed in the surface components in Figure 20 C at this point other than a weakly decreasing intensity of

adsorbed carbon, the drop in the work function can then be seen as another indication for carbon segregation into the bulk. According to that suggestion, the subsurface concentration of carbon would increase over time starting in the middle of the O-MTL. As this is the only observable change on the surface at that time, the sharply dropping conversion rate, evident by the drop in the water partial pressure, as well as the small peak in the methane partial pressure in Figure 18 B must be related to the increasing amount of subsurface carbide. This can be explained by suggesting that the subsurface carbon phase partly inhibits methane adsorption. Thus, it is proposed that the amount of subsurface carbon dictates the product of methane oxidation.

Furthermore, a surface phase can now be related to the low conversion rate at t $\approx$ 200 s, proven by the low product pressures in Figure 18 A. As the only thing changing in the surface spectra between t $\approx$ 30 s and the end of the temperature ramp is the surface oxygen signal, it can be assumed that the oxygen coverage of the surface is responsible for the changes in conversion rate observed in the gas phase spectra. When one looks at the ratio between the peak intensities of Pd bulk and Pd atoms bound to surface oxygen, the result in this study resembles the one obtained by Fernandes *et al.* in [17]. There, it was found that for this peak ratio, a surface oxide is formed. Thus, on the way from the completely removed oxide in the O-MTL to the surface oxide, the stage of a thin $\sqrt{5}$-like oxide has to be passed which is known to have a high activation energy for methane dissociation [19] and, hence, a low conversion rate. An increasingly thick oxide then seems to have a rising activity toward methane oxidation. Here, the term *activity* can be used as the temperature of the catalyst is at a constant value of 450 °C while the conversion rate obviously changes.

Finally, also an explanation for the excess formation of water seen around the O-MTL in Figure 18 B can be offered. The accumulation of adsorbed carbon at the surface is proposed to have the following origin; Methane adsorbs on metallic Pd and dissociates. Then, carbon is assembled on the surface while hydrogen reacts with the remaining oxide or oxygen, forming an excess of water. As long as the catalyst temperature is not too high, some of the excess carbon will segregate into the bulk which is why it cannot be observed as adsorbed carbon in the spectra. After exiting the O-MTL, the oxygen coverage of the surface increases again which makes it increasingly likely that adsorbed carbon reacts with oxygen to form CO_2. Therefore, H_2O and CO_2 reach the same partial pressure shortly after the catalyst temperature arrives at 450 °C and only complete combustion is observed from that point onward.

Concluding the findings reached by discussing the C 1s, O 1s, and Pd 3d surface spectra it needs to be mentioned that all the way through the O-MTL, carbon is present at the surface. The formation of this carbide phase is at the same time the reason for the excess water formation observed in the discussion of the gas phase spectra. Another finding is that the concentration of subsurface carbon seems to dictate which reaction product is formed, i.e. a low subsurface carbon concentration results in an increased conversion rate while a high concentration has a contrary effect. Finally, when analyzing the point of low conversion rate found in the discussion of the gas phase spectra, a thin $\sqrt{5}$-like oxide can be most likely held responsible for that effect.

6.3. Discussion
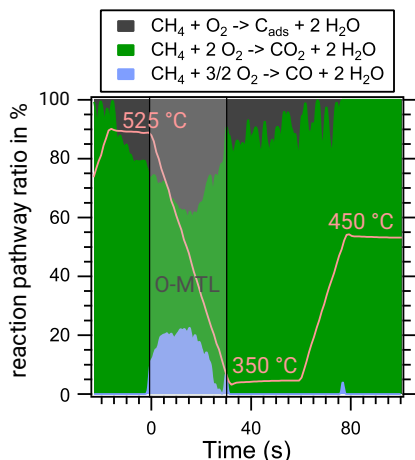
Figure 22: *Deducted development of the reaction pathway profile.*

From the discussion of the time-resolved surface spectra, it is evident that carbon deposition takes place, while the time-resolved gas phase spectra report complete and partial combustion of methane. Using the time-resolved gas phase spectra, the percentage of methane that is processed via each reaction channel can be calculated. As the same amount of water is produced for every reaction pathway, the partial pressure signal of water is a measure for the total methane conversion, assuming that no H_2 in the gas phase is formed. This is a reasonable assumption as H_2 is very unlikely to co-exist with molecular oxygen.

The CO_2 signal will then result from complete combustion while the CO signal can only come from partial combustion. The remaining water signal after subtracting these two contributions must then be the result of carbon deposition. With these assumptions, the amount of methane being processed via each reaction channel can be calculated and is shown in Figure 22. During the calculations, a threshold was applied to the sum of every two consecutive data points. If the sum was higher than the threshold, these data points were added to the plot, otherwise, their values were set to zero.

In the resulting plot, a key observation is that the carbon deposition on the surface is present within a longer time range around the oxygen MTL whereas the CO production is limited to the O-MTL. Furthermore, an explanation for the long tail in the carbon deposition, i.e. between 30 s and roughly 80 s, as compared to the quicker onset before the O-MTL, i.e. from -20 s through 0, can be offered. These observations fit well with the scenario of methane dissociation on metallic Pd sites, depositing carbon and producing hydrogen. Thus, while enough metallic Pd sites are available with too little oxygen in the vicinity to react with carbon, this reaction will happen. CO, however, is only produced when there is a total shortage in the supply of oxygen. The subsurface carbide that is assembled during this process is assumed to stay subsurface, accumulating more and more carbon over several of these cycles. Thus, the bulk of the catalyst is gradually filled up with carbon which, eventually, will lead to a decreasing activity. This assumption stems from the observation within the discussion of the gas phase spectra, that the amount of subsurface carbon will dictate the chosen reaction pathway. The reduction in conversion rate was even observed during the beamtime (results are not presented here) where the process continued until the reaction did not enter into the O-MTL anymore. Then, the subsurface carbon had to be removed by oxidizing the catalyst at high temperatures for a short time span, e.g. 5 minutes, and the initial behavior could be reproduced again. Over short enough timescales, i.e. 50-70 min, the ramps were similar enough (see appendix). Proof for this theory could be obtained by studying the system with some of the techniques discussed in the outlook.

34

Finally, when all the previously acquired knowledge is combined, a model of the surface development and its methane conversion properties during one temperature ramp can be built. The result is shown in Figure 23.

At the beginning of the temperature ramp, at 450 °C, the palladium catalyst is covered mainly by a multilayer oxide. When the temperature rises, the oxygen coverage becomes smaller and metallic palladium is exposed to CH_4, leading to carbon deposition. This oxide reduction is most likely a chemically driven effect, i.e. the oxide reacts with methane to form water and carbon dioxide. The reduction is a rather quick development which was predicted by the jump in the work function shift, seen in the apparent binding energy of the gas phase components. It is suggested that carbon deposition starts even before all surface oxygen is removed. This deposited carbon segregates into the bulk but then, at a sufficiently high carbon deposition rate, results in a buildup of carbide and adsorbed CO on the surface until the temperature is low enough to allow segregation of higher amounts of carbon into the bulk again as well as lowering the overall carbon deposition. Decreasing the temperature further leads to reduced carbon deposition as well as faster carbon segregation into the bulk and CO desorption into the gas phase. Despite the temperature reduction from 525 °C to 350 °C the carbide surface is active enough to keep the surface in the O-MTL, indicated by CO production.
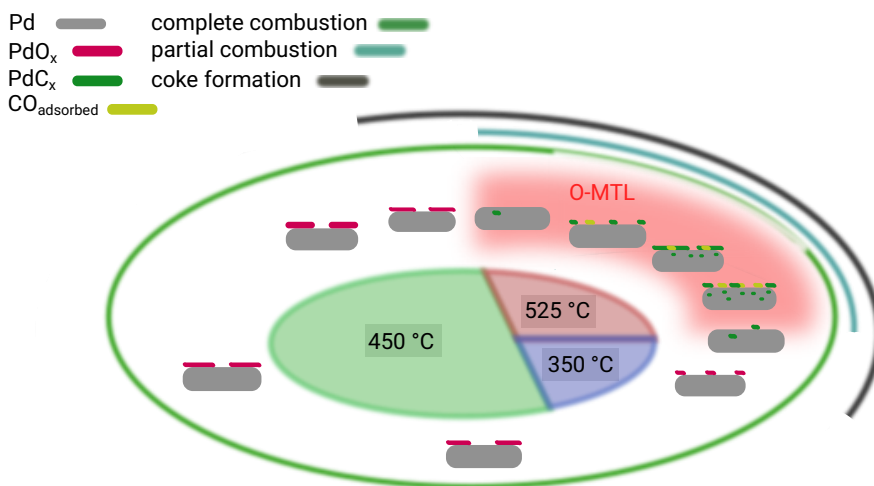
Figure 23: *Simplified representation of the proposed development of the Pd surface* while applying a temperature ramp. The associated reaction pathway profile is denoted as well.

When exiting the O-MTL, all surface carbon is removed and the metallic palladium surface is observed again, displaying a similar methane conversion profile as before even though the catalyst is at a lower temperature now. While staying at 350 °C, oxygen adsorption starts and an oxide builds up. The methane conversion rate decreases while more and more oxygen is assembled on the surface and the carbon deposition rate decreases. This development seems to be unaffected by the change of temperature to 450 °C. When a certain oxygen coverage

of the surface is reached, few metallic Pd sides are available for methane adsorption, and the turnover frequency reaches a minimum. When the oxide grows thicker, the methane conversion rate rises again. This suggested cycle with the corresponding effects in the methane conversion rate of the surface phase agrees with the findings in [25], [6], [26], and [15].

When analyzing the data, it has to be taken into consideration that, the gas exchange in the vicinity of the sample does not happen instantly. Assuming, however, that the highly active catalyst does not immediately transform into a completely inactive catalyst, but rather anticipating a gradual change, likewise, no immediate changes in the gas phase are expected.

Hence, the key observations of the experiment are that the O-MTL is accompanied by a surface carbide phase and that a thin surface oxide of a certain surface coverage is present when the conversion rate is low. Furthermore, when keeping the catalyst at a constant temperature, i.e. 450 °C, the surface oxide grows thicker, and a gradually increasing conversion rate is displayed. Another key observation is that carbon deposition happens for a much longer time than just in the oxygen MTL while partial combustion of methane is clearly restricted to that time frame. Interestingly, here, the concentration of subsurface carbon seems to dictate the reaction pathway profile. That means that a little bit of subsurface carbon results in an increased methane conversion rate while much of it inhibits methane adsorption, leading to a sharp decrease in the conversion rate in the middle of the O-MTL. If the fact, that subsurface carbon has such a decisive importance, can be verified in future studies, it would definitely be a very interesting result.

7. Conclusion and Outlook

Methane oxidation over a polycrystalline Pd catalyst was studied in both, a methane-rich, and a balanced gas environment of roughly 5 mbar. Here, the core levels of all participating atoms, i.e. O 1s, C 1s, and Pd 3d, were measured while applying a temperature ramp to the catalyst between 350 °C and 585 °C. Thus, transitions in the catalyst surface phase were observed between various oxides, a metallic surface, and a Pd carbide surface.

In the first experiment conducted, various thick surface oxides were studied while the second experiment focused on thin oxides, carbides, and metallic surfaces. While studying methane oxidation over various Pd oxide surface phases, it became evident that all methane is processed via complete combustion, i.e. forming CO_2 and H_2O. When the oxide is reduced and more and more metallic Pd sites become available for methane dissociation, carbon deposition is observed. That means that the carbon atom segregates into the bulk of the Pd catalyst before a reaction with oxygen can happen. An increasing methane conversion rate then leads to the removal of the surface oxide, and, with the reaction being mass transfer limited by oxygen, a surface carbide phase is built up. As long as that phase is detected, carbon deposition is strongly present as well as a diminished percentage of complete combustion, and partial combustion, forming CO can be observed. Here, the concentration of subsurface carbon, i.e. surface carbon that segregates into the bulk of the catalyst, seems to dictate the reaction pathway profile. That means that a little bit of subsurface carbon results in an increased methane conversion rate while much of it inhibits methane adsorption, leading to a sharp decrease in the conversion rate. Importantly, some of these results, such as those based on the water signal development, would have been missed using other techniques such as tr-QMS measurements for the gas phase composition. Additionally, the results involving the study of the surface layers of the catalyst, such as when discussing the carbon coverage, would have been missed using a very bulk-sensitive technique. These two facts again prove the value of tr-APXPS.

Having summarized the results of the study, it is discussed how future experiments could improve the results obtained in this thesis. First and foremost, the electron analyzer's detector transmission function needs to be mentioned. When measuring the spectra in screenshot mode, capturing the transmission function will make it possible to introduce a smaller error in the comparison of peak intensities. A second improvement would be capturing the same spectra for different photon energies, to make depth profiling possible. Continuing to study the experimental system presented in this thesis with APXPS, the temperature pulsing method can be applied in a more rapid fashion. Instead of measuring and evaluating one temperature ramp, several hundred pulses can be fired. The very periodic behavior of the surface, and the respective answer of the gas phase, can then be used for event-averaging purposes as presented by Knudsen *et al.* in [11]. This can provide the researcher with a much higher signal-to-noise ratio when analyzing the developments during one pulse. The reader may recall that some spectra, mostly the O 1s surface spectra, had to be binned severely during the analysis presented in this thesis, and even then, the analysis was not always possible. Thus, an improved signal-to-noise ratio would have a large impact on this study as the development of the surface oxide for instance could be studied in much more detail.

Additionally, the same system could be studied using other surface science techniques which can then provide even deeper knowledge about the system. One possibility would be to study the same system with Hard X-ray Photoelectron Spectroscopy (HAXPES), probing for instance the development of the bulk concentration of carbon during one temperature cycle. Using different photon energies, this can even be studied for different depths of the catalyst. SXRD can give more insight into the real surface phase and its structure instead of relying on the small differences in binding energy. Surface Optical Reflectance (SOR) will then additionally provide information about the thickness of the surface phase. Planar Laser-Induced Fluorescence (PLIF) can be used to determine the concentration gradient of reactants or products over the catalyst surface and thus provide more information about the MTL of the reaction. Ultraviolet Photoelectron Spectroscopy (UPS) can be used to study the electronic structure of the surface, thus finally eradicating whether structural or electronic changes of the surface trigger changes in the reaction pathway profile. This method can even detect hydrogen molecules and could thus verify or falsify the assumption, that no gas phase H_2 is formed in this reaction.

Overall, this thesis, bridging the materials and pressure gap, could explicitly relate certain surface phases to the respective profile of specific reaction pathways with a high time resolution (0.2 s), i.e. how much reactant is processed via which reaction channel. These results, especially the fact that carbon deposition already takes place when there is still oxide at the surface, might prove highly relevant for industrial applications. For instance, catalysts can then be used in gas composition regimes where rapid degradation of the catalyzing performance must not be risked due to an increasing subsurface carbide. Furthermore, acquiring spectra rapidly while ramping the temperature to enforce transitions in the catalyst's surface is demonstrated to be a powerful method. The successes of this technique open up further research in catalysis, for instance when studying alloy catalysts. There, periodically enforcing changes in the surface component can, for instance, enable detailed studies of the active component in the alloy.

Therefore, in conclusion, the value of the thesis is two-fold. First of all, it gives a directive on the gas environments Pd catalysts have to be operated in to achieve certain reaction products. On a more indirect account, however, the technique of temperature ramping used is demonstrated to be a powerful method of which the application need not only be limited to heterogeneous catalysis. These contributions will, in the long run, help the fabrication of suitable catalysts that can be used to remove traces of methane in unburned fuel in biogas engines. Those are going to replace the engines based on fossil fuels more and more in the coming decades.

Bibliography

1. Zhang, S. *et al.* In situ studies of surface of NiFe2O4 catalyst during complete oxidation of methane. *Surface Science* **648.** Special issue dedicated to Gabor Somorjai's 80th birthday, 156–162. ISSN: 0039-6028. `https://www.sciencedirect.com/science/article/pii/S0039602815004136` (2016).

2. Dou, J. *et al.* Complete Oxidation of Methane on Co3O4/CeO2 Nanocomposite: A Synergic Effect. *Catalysis Today* **311.** SI: C1 Catalysis, 48–55. ISSN: 0920-5861. `https://www.sciencedirect.com/science/article/pii/S0920586117308465` (2018).

3. Schnadt, J., Knudsen, J. & Johansson, N. Present and new frontiers in materials research by ambient pressure x-ray photoelectron spectroscopy. *Journal of Physics: Condensed Matter* **32,** 413003. `https://doi.org/10.1088/1361-648x/ab9565` (July 2020).

4. Pfaff, S. *On the Chemical Romance Between Gas and Surface, and how to Illuminate it* PhD thesis (Lund University, 2022).

5. Boix, V. *Graphene: Applications in Surface Science Studies* English. Defence details Date: 2022-12-02 Time: 13:15 Place: Rydbergsalen, Department of Physics. External reviewer(s) Name: Martín-Gago, José Ángel Title: Professor Affiliation: Instituto de Ciencia de Materiales de Madrid-CSIC (ICMM-CSIC) —. PhD thesis (Synchrotron Radiation Research, October 2022). ISBN: 978-91-8039-447-5.

6. Bluhm, H. *et al.* In Situ X-Ray Photoelectron Spectroscopy Studies of Gas-Solid Interfaces at Near-Ambient Conditions. *MRS Bulletin* **32,** 1022–1030 (2007).

7. Hüfner, S. *Photoelectron Spectroscopy* (Springer Verlag, Berlin Heidelberg, 2003).

8. Starr, D. E., Liu, Z., Hävecker, M., Knop-Gericke, A. & Bluhm, H. Investigation of solid/vapor interfaces using ambient pressure X-ray photoelectron spectroscopy. *Chemical Society Review,* 5833–5857. `https://doi.org/10.1039/C3CS60057B` (2013).

9. Ogletree, D. F. *et al.* A differentially pumped electrostatic lens system for photoemission studies in the millibar range. *Review of Scientific Instruments* **73,** 3872–3877. eprint: `https://doi.org/10.1063/1.1512336`. `https://doi.org/10.1063/1.1512336` (2002).

10. Stakheev, A., Batkin, A. & Teleguina, N. Particle Size Effect on CH4 Oxidation Over Noble Metals: Comparison of Pt and Pd Catalysts. *Top Catal* **56,** 306–310. `https://doi.org/10.1007/s11244-013-9971-y` (2013).

11. Knudsen, J. *et al.* Stroboscopic operando spectroscopy of the dynamics in heterogeneous catalysis by event-averaging. *Nature Communications* **12,** 6117. ISSN: 2041-1723 (2021).

12. Zhu, S. *et al.* HIPPIE: a new platform for ambient-pressure X-ray photoelectron spectroscopy at the MAX IV Laboratory. *Journal of Synchrotron Radiation* **28,** 624–636. `https://doi.org/10.1107/S160057752100103X` (March 2021).

13. Rodriguez, J. A., Rui, N., Zhang, F. & Senanayake, S. D. In Situ Studies of Methane Activation Using Synchrotron-Based Techniques: Guiding the Conversion of C–H Bonds. *ACS Catalysis* **12.** doi: 10.1021/acscatal.2c00941, 5470–5488 (2022).

14. Zheng, G. & Altman, E. The oxidation mechanism of Pd(100). *Surface Science* **504,** 253–270. ISSN: 0039-6028. `https://www.sciencedirect.com/science/article/pii/S0039602802011044` (2002).

15. Bychkov, V., Tyulenin, Y., Gorenberg, A., Sokolov, S. & Korchak, V. Evolution of Pd catalyst structure and activity during catalytic oxidation of methane and ethane. *Applied Catalysis A: General* **485,** 1–9. ISSN: 0926-860X. `https://www.sciencedirect.com/science/article/pii/S0926860X1400458X` (2014).

16. CAMPBELL, J. & PAPP, T. WIDTHS OF THE ATOMIC K–N7 LEVELS. *Atomic Data and Nuclear Data Tables* **77,** 1–56. ISSN: 0092-640X. `https://www.sciencedirect.com/science/article/pii/S0092640X00908489` (2001).

17. Fernandes, V. R. *et al.* Reversed Hysteresis during CO Oxidation over Pd75Ag25(100). *ACS Catalysis* **6.** doi: 10.1021/acscatal.6b00658, 4154–4161 (2016).

18. Westerström, R. *et al.* Oxidation and reduction of Pd(100) and aerosol-deposited Pd nanoparticles. *Phys. Rev. B* **83,** 115440. `https://link.aps.org/doi/10.1103/PhysRevB.83.115440` (11 March 2011).

19. Hellman, A. *et al.* The Active Phase of Palladium during Methane Oxidation. *The Journal of Physical Chemistry Letters* **3.** PMID: 26286272, 678–682. eprint: `https://doi.org/10.1021/jz300069s`. `https://doi.org/10.1021/jz300069s` (2012).

20. Goodwin, C. M. *et al.* The Structure of the Active Pd State During Catalytic Carbon Monoxide Oxidization. *The Journal of Physical Chemistry Letters* **12.** PMID: 33955763, 4461–4465. eprint: `https://doi.org/10.1021/acs.jpclett.1c00620`. `https://doi.org/10.1021/acs.jpclett.1c00620` (2021).

21. Zetterberg, J. *et al.* Spatially and temporally resolved gas distributions around heterogeneous catalysts using infrared planar laser-induced fluorescence. *Nature communications* **6,** 7076 (2015).

22. Li, Y. *et al.* CO oxidation over graphene supported palladium catalyst. *Applied Catalysis B: Environmental* **125,** 189–196. ISSN: 0926-3373. `https://www.sciencedirect.com/science/article/pii/S0926337312002263` (2012).

23. Bowker, M. *et al.* Carbon Dissolution and Segregation in Pd(110). *The Journal of Physical Chemistry C* **114,** 5060–5067. eprint: `https://doi.org/10.1021/jp9108046`. `https://doi.org/10.1021/jp9108046` (2010).

24. Ratajczykowa, I. Carbon segregation to the Pd(111) single crystal surface as seen in carbon monoxide thermal desorption spectra. *Journal of Vacuum Science & Technology A* **1,** 1512–1517. eprint: `https://doi.org/10.1116/1.572177`. `https://doi.org/10.1116/1.572177` (1983).

25. Kaichev, V. V., Vinokurov, Z. S. & Saraev, A. A. Self-sustained oscillations in oxidation of methane over palladium: the nature of "low-active" and "highly active" states. *Catal. Sci. Technol.* **11,** 4392–4397. `http://dx.doi.org/10.1039/D1CY00132A` (13 2021).

26. Peskov, N., Slinko, M., Bychkov, V. & Korchak, V. Mathematical modelling of oscillatory behaviour during methane oxidation over palladium catalysts. *Chemical Engineering Science* **84,** 684–694. ISSN: 0009-2509. `https://www.sciencedirect.com/science/article/pii/S0009250912005763` (2012).

8. Acknowledgements

9. Appendix

9.1. Background Removal

```
function BackgroundRemoval1(original)
wave original
string name=Nameofwave(original)

// IntImage (after placing cursor in image)
duplicate $name+"Int" $name+"WB"
wave filenameWB = $name+"WB"
filenameWB=0

appendToGraph /R filenameWB //(append it to right axis)
// RUN THE FOLLOWING COMMANDS MANUALLY
// filenameWB[pcsr(B),pcsr(A)]=1
// select new Background points, run command again
// open Analysis → curve fitting
// select function → poly
// from Target, X-data: calculated, Y-data: filenameInt, Weighting: filenameWB
end

function BackgroundRemoval2(original)
wave original
string name=Nameofwave(original)
wave W_coef

duplicate /o $name $name+"Bgr"
wave filenameBgr=$name+"Bgr"
filenameBgr=poly(W_coef,x)
duplicate /o $name $name+"WOBgr"
wave filenameWOBgr=$name+"WOBgr"
filenameWOBgr[][]=original-filenameBgr
display; appendimage filenameWOBgr

end
```

9.2. Calibrate to Fermi Edge

```
function FEcalib(original,fermi)
// original has to have background already removed
wave original, fermi
string nameOrig, nameFermi
```

```
nameOrig = Nameofwave(original)
nameFermi = Nameofwave(fermi)

duplicate /o fermi fermi_smooth

smooth 20, fermi_smooth
differentiate fermi_smooth
curvefit /Q gauss, fermi_smooth
wave W_coef

// to obtain the position of the Fermi Edge and its width,
// we differentiate the data and fit a gaussian to it. The peak position
// is then the Fermi Edge and the FWHM its width.

variable FE_guess, xmax, xmin

FE_guess = W_coef[2] //estimates the first guess for FE
//estimates the first point to usw in the FE fit
xmin = x2pnt(fermi, (W_coef[2]-2*1.35*W_coef[3]/sqrt(2)))
//estimates the last point to use in the FE fit
xmax = x2pnt(fermi, (W_coef[2]+2*1.35*W_coef[3]/sqrt(2)))

wavestats/Q fermi
W_coef[0]={V_min, V_max-V_min,FE_guess,0.1} // set starting values for the fit with
// bounds being the lowest and highest kinetic energy, peak
// position being the initial FE guess and 0.1 being the width of the gaussian

 // fit a step function to the FE data within the previously defined bounds
 // using the starting values
Funcfit/Q ErfStep W_coef fermi[xmin,xmax]

duplicate/o fermi fermi_fit

fermi_fit = ErfStep(W_coef,x)

display fermi, fermi_fit
ModifyGraph mode($nameofwave(fermi))=2,rgb($nameofwave(fermi))=(0,0,0)
ModifyGraph lsize($nameofwave(fermi))=2

//The fermi edge callibrated is the w[2] of the error function fitted.

Print "Fermi edge = " + num2str(W_coef[2]) +" eV"
```

```
//Now we callibrate the wave without background to the FE

variable Fedge, Startpoint, dx
Fedge = W_coef[2]

Startpoint = pnt2x(original,0) // returns the X value at the point 0 of the
    //wave original
dx = pnt2x(original,1)-pnt2x(original,0)

duplicate/o original $nameOrig+"_FEC"

wave original_fec=$nameOrig+"_FEC"

//-------------------------------- get Excitation energy from metadata
string excEnergy_string=GetNote($nameOrig, "Excitation Energy")
variable excEnergy=str2num(excEnergy_string)

print "Excitation Energy = " + num2str(excEnergy) + "eV"

//------------------------- do case differentiation depending on whether or not
// the file has already been changed to binding energy scale
variable BindingE_offset=excEnergy-Fedge
print "Binding Energy offset = "+ num2str(BindingE_offset) + "eV"
string EnergyScale=GetNote($nameOrig, "Energy Scale")

if (stringmatch(EnergyScale,"Binding"))
setscale /p x, Startpoint-BindingE_offset, dx, original_fec
elseif(stringmatch(EnergyScale,"Kinetic"))
setscale /p x, Fedge-Startpoint, dx, original_fec
else
print "neither binding energy nor kinetic energy scale"
endif

display original, original_fec
ModifyGraph rgb($nameofwave(original))=(0,0,0)

//Now we display the final wave alone:

display; appendimage original_fec
//Autoscale and flip axis of the new spectra (lower BE to the right)
SetAxis/A/R bottom
```

```
End


//----------Step function--------------------

//Function ErfStep(w,x) : FitFunc
// wave w
// variable x
// return w[0]+w[1]*erf((x-w[2])/w[3])
//end

Function/S GetNote(wavenm,noteKey)
    WAVE wavenm
    string noteKey
    return stringbykey(noteKey,note(wavenm),"=","\r")[0,inf]
end

Function SetNote(wavenm, noteKey, newValueStr)
    WAVE wavenm
    string noteKey
    string newValueStr

    if(stringmatch(newValueStr,""))
        note/k wavenm, removebykey(noteKey,Note(wavenm),"=","\r")
    else
        note/k wavenm, replacestringbykey(noteKey,Note(wavenm),
        " "+newValueStr,"=","\r")
    endif
end
```

9.3. Fit Code

```
macro JustFit(startvalue,framevalue,name_orig,binned)

string name_orig, binned, helpflag
variable startvalue, framevalue
string moviename, wavetoplot, sourcewave, holdstring
variable i, LeftP, RightP, nbrofframes, start, g
variable V_FitError=0
variable/G answerCompare

sourcewave= name_orig //CsrWave(A)
```

```
moviename=sourcewave+"_movie"
wavetoplot="Plotwave1"

getaxis /q left
start=startvalue //y-value of wave to be started with
i=start //set counter value on start position
nbrofframes=framevalue //number of waves to be put into movie


duplicate /O /R=[][i] $sourcewave $wavetoplot

//Make/D/N=(nbrofframes)/O W_coef
Make/D/N=41/O W_coef_matrix
Make/D/N=200/O newfitwave
newfitwave=0

  W_coef= //define inital guess of components


do

print "iteration "+num2str(i-start)+" of "+num2str(nbrofframes)

$wavetoplot=$sourcewave[p][i]

// Function Fit
Getaxis /q bottom

//LeftP=scaletoIndex($wavetoplot,V_min,0)
RightP=scaletoIndex($wavetoplot,V_max,0)
LeftP=0

if (i-start<=3)
//fit peak positions
Make/O/T/N=8 T_Constraints
// define constraints on possible binding energies for the individual peaks
T_Constraints = {"K3 > 530", "K3<532","K7 > 532", "K7<533.4","K11 > 534.2",
                 "K11<535.13", "K15 > 535.93", "K15<536.48"}
V_FitError=0
holdstring="1110111011101110111111111111111111111111"
FuncFit/q/H=holdstring TenVoigtsSymmetric W_coef $wavetoplot[LeftP,RightP]
                /D /C=T_Constraints
        if (V_FitError & 2) // a singular matrix error
```

```
                 print "problem in peak position fitting"
         endif

//fit peak intensities
holdstring="10111011101110111111111111111111111111111"
Make/O/T/N=3 T_Constraints
T_Constraints = {"K1 > 0","K5 > 0","K9 > 0","K13>0"}
V_FitError=0
FuncFit/q/H=holdstring TenVoigtsSymmetric W_coef $wavetoplot[LeftP,RightP]
                 /D /C=T_Constraints


//fit width
Make/O/T/N=4 T_Constraints
T_Constraints = {"K2 > 0","K6 > 0","K10 > 0","K14 > 0"}
V_FitError=0
holdstring="11011101110111011111111111111111111111111"
FuncFit/q/H=holdstring TenVoigtsSymmetric W_coef $wavetoplot[LeftP,RightP]
                 /D /C=T_Constraints
if (V_FitError)
        if (V_FitError & 2) // a singular matrix error
            print "problem in peak width fitting"
        endif
endif

else
// start fitting the rest of the 2D image
//fit peak positions
// differentiate between cases where some peaks only appear in certain regions
if (stringmatch(binned,"y"))
if(i<=119)
helpflag="beforeWFshift"
endif
comparevalues(i,119,159)
if(answerCompare==1)
helpflag="afterWFshift"
endif
comparevalues(i,159,1404)
if(answerCompare==1)
helpflag="beforeWFshift"
endif
comparevalues(i,1404,1439)
if(answerCompare==1)
```

```
helpflag="afterWFshift"
endif
comparevalues(i,1439,2576)
if(answerCompare==1)
helpflag="beforeWFshift"
endif
comparevalues(i,2576,2609)
if(answerCompare==1)
helpflag="afterWFshift"
endif
if(i>2609)
helpflag="beforeWFshift"
endif
else
if(i<=478)
helpflag="beforeWFshift"
endif
comparevalues(i,478,639)
if(answerCompare==1)
helpflag="afterWFshift"
endif
if(i>639)
helpflag="beforeWFshift"
endif
endif
if(stringmatch(helpflag,"beforeWFshift"))
Make/O/T/N=8 T_Constraints
T_Constraints = {"K3>531.4","K3<531.68","K7>532.85","K7<533.05","K11>535.0",
                    "K11<535.3", "K15>536","K15<536.37"}
holdstring="11101110111011101111111111111111111111"
endif
if(stringmatch(helpflag,"afterWFshift"))
Make/O/T/N=6 T_Constraints
T_Constraints = {"K3>531.83","K3<532.16","K7>533.22","K7<533.64","K39>534.28",
                    "K39<534.9"}
holdstring="11101110111111111111111111111111111101"
endif


helpflag=""
V_FitError=0
FuncFit/q/H=holdstring TenVoigtsSymmetric W_coef $wavetoplot[LeftP,RightP]
                    /D /C=T_Constraints
```

```
    if (V_FitError & 2) // a singular matrix error
     print "problem in peak position fitting"
     endif


//fit peak intensities
// try fitting all intensities first
holdstring="1011101110111111111111111111111111110111"
Make/O/T/N=4 T_Constraints
T_Constraints = {"K1 > 0.001","K5 > 0.001","K9 > 0.001","K37>0.001"}
V_FitError=0
FuncFit/q/H=holdstring TenVoigtsSymmetric W_coef $wavetoplot[LeftP,RightP]
                        /D /C=T_Constraints
        if (V_FitError & 2) // a singular matrix error
            print "problem in peak intensity fitting"
            // if there is a problem in this fit, only fit those values
            // that are not leading to singular matrices
            holdstring=""
            T_Constraints={"1"}
             if (W_coef[1]<0.001)
W_coef[1]=0.001
    holdstring=holdstring+"11111"
    print "1 is a problem"
else
holdstring=holdstring+"10111"
Make/O/T/N=(dimsize(T_Constraints,0)+1) T_help
T_help[dimsize(T_help,0)] = {"K1>0.001"}
T_Constraints=T_help
endif
if (W_coef[5]<0.001)
W_coef[5]=0.001
    holdstring=holdstring+"1111"
    print "5 is a problem"
else
holdstring=holdstring+"0111"
Make/O/T/N=(dimsize(T_Constraints,0)+1) T_help
T_help[dimsize(T_help,0)] = {"K5>0.001"}
T_Constraints=T_help
endif
if (W_coef[9]<0.001)
W_coef[9]=0.001
    holdstring=holdstring+"1111"
    print "9 is a problem"
else
```

```
holdstring=holdstring+"0111"
Make/O/T/N=(dimsize(T_Constraints,0)+1) T_help
T_help[dimsize(T_help,0)] = {"K9>0.001"}
T_Constraints=T_help
endif
if (W_coef[13]<0.001)
W_coef[13]=0.001
    holdstring=holdstring+"111111111111111111111111111"
    print "13 is a problem"
else
holdstring=holdstring+"011111111111111111111111111"
Make/O/T/N=(dimsize(T_Constraints,0)+1) T_help
T_help[dimsize(T_help,0)] = {"K13>0.001"}
T_Constraints=T_help
endif
if (W_coef[37]<0.001)
W_coef[37]=0.001
    holdstring=holdstring+"1111"
    print "37 is a problem"
else
holdstring=holdstring+"0111"
Make/O/T/N=(dimsize(T_Constraints,0)+1) T_help
T_help[dimsize(T_help,0)] = {"K37>0.001"}
T_Constraints=T_help
endif
g = 0
if (dimsize(T_Constraints,0)==1)
V_FitError=0
FuncFit/q/H=holdstring TenVoigtsSymmetric W_coef $wavetoplot[LeftP,RightP] /D
else
Make /D/T/N=(dimsize(T_Constraints,0)-1) /o T_help
do
T_help[g]=T_Constraints[g+1]
g=g+1
while(g<dimsize(T_Constraints))
T_Constraints=T_help
V_FitError=0
FuncFit/H=holdstring TenVoigtsSymmetric W_coef $wavetoplot[LeftP,RightP]
                                /D /C=T_Constraints
endif
        endif
endif
```

```
//fill fit coefficients into matrix
duplicate /o W_coef_matrix helpmatrix
concatenate/o {helpmatrix,W_coef}, W_coef_matrix
killwaves helpmatrix

duplicate /o newfitwave helpmatrix
concatenate/o {helpmatrix,fit_Plotwave1}, newfitwave
killwaves helpmatrix

i=i+1


while(i<start+nbrofframes)

DeletePoints/M=1 0, 1, W_coef_matrix


//print W_coef_matrix

end

function comparevalues(counter,v1,v2)
variable v1, v2, counter
NVAR answerCompare = root:answerCompare
if(counter>v1&&counter<v2)
answerCompare=1
else
answerCompare=0
endif
return answerCompare
end
```

9.4. Fit Functions

```
Function VoigtIgor93(X,Y) :FitFunc
// Voigt function obtained from Igor users group Sep 93
variable X,Y                        // see acompanying word file for details

variable/C W,U,T= cmplx(Y,-X)
variable S =abs(X)+Y

if( S >= 15 )
W= T*0.5641896/(0.5+T*T)
```

```
else
if( S >= 5.5 )
U= T*T
W= T*(1.410474+U*0.5641896)/(0.75+U*(3+U))
else
if( Y >= (0.195*ABS(X)-0.176) )
W= (16.4955+T*(20.20933+T*(11.96482+T*(3.778987+T*0.5642236))))
W /= (16.4955+T*(38.82363+T*(39.27121+T*(21.69274+T*(6.699398+T)))))
else
U= T*T
W=T*(36183.31-U*(3321.9905-U*(1540.787-U*(219.0313-U*
                                    (35.76683-U*(1.320522-U*0.56419))))))
W /=(32066.6-U*(24322.84-U*(9022.228-U*(2186.181-U*
                                    (364.2191-U*(61.57037-U*(1.841439-U)))))))
W= cmplx(exp(real(U))*cos(imag(U)),0)-W
endif
endif
endif
return real(W)
end
// Voigt Fit Functions
// Parameters:
// First peak:
// w[0]: linear background
// w[1]: intensity
// w[2]: width parameter
// w[3]: line position
// w[4]: proportion lorentzian (0=pure Gaussian)
// (w[5]: asymmetry parameter (0=symmetric) )
// The other peaks according to the same scheme.
//
// The Gaussian HALF width (at half maximum) is given by sqrt(ln(2))/w[2].
// The Lorentzian HALF width (at half maximum) is given by w[4]/w[2].
// The area under the peak is given by w[1]*sqrt(Pi)/w[2].
// The Voigt HALF width (at half maximum, SYMMETRIC PEAKS ONLY) is given by
//  w[4]/w[2]+sqrt((w[4]/w[2])^(4/2)+(sqrt(ln(2))/w[2])^2).

//
// Functions that handle TEN Voigtfunctions
//

Function TenVoigtsSymmetric(w,x) : FitFunc
Wave w
```

```
Variable x

Variable Voigt1,Voigt2,Voigt3,Voigt4,Voigt5,Voigt6,Voigt7,Voigt8,Voigt9,Voigt10

Voigt1=abs(w[1])*voigtIgor93(w[2]*(x-w[3]),w[4])
Voigt2=abs(w[5])*voigtIgor93(w[6]*(x-w[7]),w[8])
Voigt3=abs(w[9])*voigtIgor93(w[10]*(x-w[11]),w[12])
Voigt4=abs(w[9]*w[13])*voigtIgor93(w[14]*(x-w[15]),w[16])
Voigt5=abs(w[17])*voigtIgor93(w[18]*(x-w[19]),w[20])
Voigt6=abs(w[21])*voigtIgor93(w[22]*(x-w[23]),w[24])
Voigt7=abs(w[25])*voigtIgor93(w[26]*(x-w[27]),w[28])
Voigt8=abs(w[29])*voigtIgor93(w[30]*(x-w[31]),w[32])
Voigt9=abs(w[33])*voigtIgor93(w[34]*(x-w[35]),w[36])
Voigt10=abs(w[37])*voigtIgor93(w[38]*(x-w[39]),w[40])

return w[0]+voigt1+voigt2+voigt3+voigt4+voigt5+voigt6+voigt7+voigt8+voigt9+voigt10

End
```
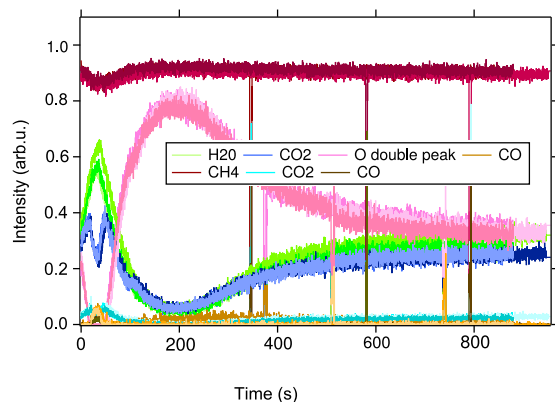
9.5. Reproducible Ramps
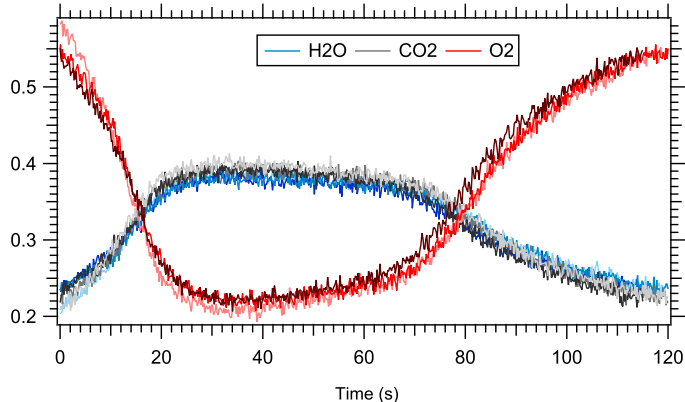
Figure 24: *Comparison of intensities for all three ramps* for A) the study where the catalyst is placed in a methane-rich environment and for B) the study where the catalyst is placed in a balanced environment.
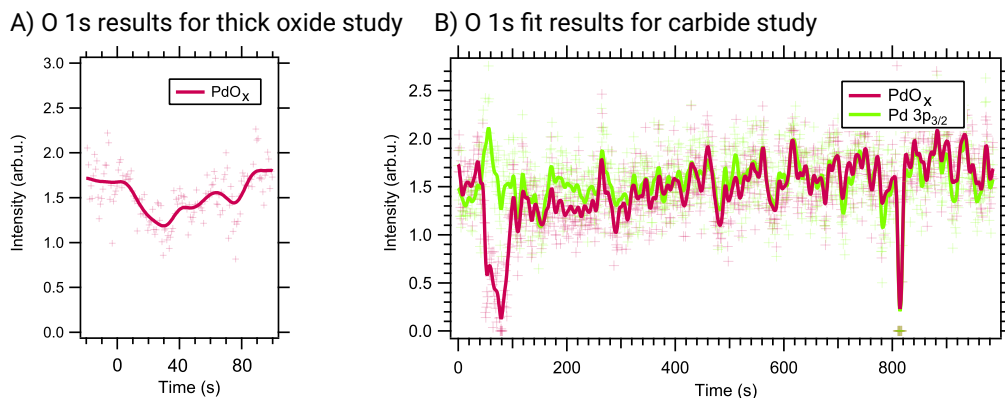
9.6. O 1s surface fit results

Figure 25: *O 1s surface fit results* for the experiment in a methane-rich environment.

9.7. Pd 3d surface component

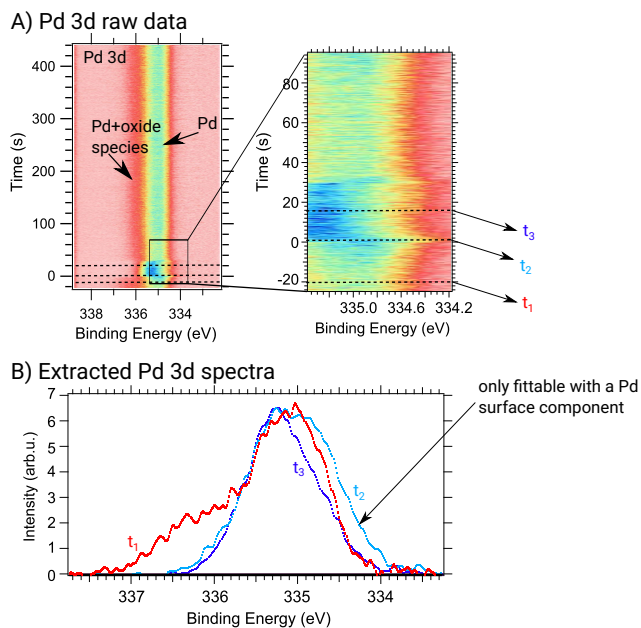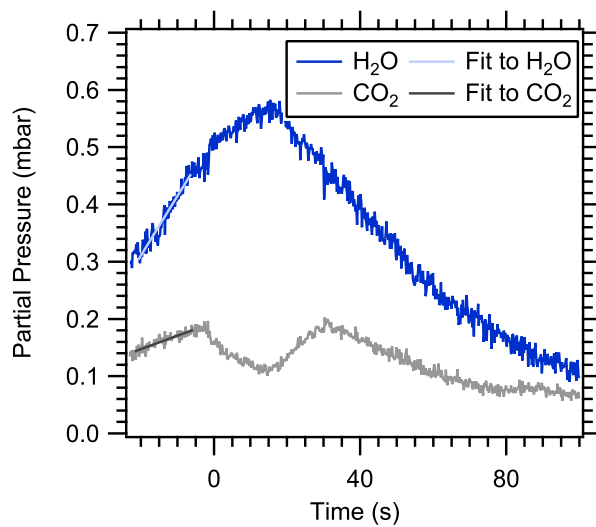**Figure 26:** *Evidence for the existence of a surface component in the Pd 3d data.*

9.8. Slopes of Partial Pressures

Figure 27: *Fits for calculating the slopes* *for the increasing gas phase pressures.*